Acoustic, Thermal and Non-thermal Dynamics in Condensed Matter Studied by Time-Resolved X-ray Diffraction

Ekström, Carl

2020

Acoustic, Thermal and Non-thermal Dynamics in Condensed Matter Studied by Time-Resolved X-ray Diffraction

CARL EKSTRÖM | FACULTY OF ENGINEERING | LUND UNIVERSITY

Printed by Media-Tryck, Lund 2020 NORDIC SWAN ECOLABEL 3041 0903

LUND UNIVERSITY
Faculty of Engineering, LTH
Department of Physics
Divison of Atomic Physics

ISBN: 978-91-7895-508-4 (print)
ISBN: 978-91-7895-509-1 (pdf)
ISSN 0281-2762
Lund Reports on Atomic Physics, LRAP 566 (2020)

Acoustic, Thermal and Non-thermal Dynamics in Condensed Matter Studied by Time-Resolved X-ray Diffraction

Acoustic, Thermal and Non-thermal Dynamics in Condensed Matter Studied by Time-Resolved X-ray Diffraction

Carl Ekström

LUND
UNIVERSITY

Thesis for the degree of Doctor of Philosophy
Thesis advisor: Prof. Jörgen Larsson. Co-advisor: Dr. Henrik Enquist
Faculty opponent: Prof. Martin Meedom Nielsen

To be presented, with the permission of the Faculty of Engineering of Lund University, for public criticism in the Rydberg Lecture Hall at the Department of Physics on Friday, 18 September, 2020 at 09:15.

Organization	Document name
LUND UNIVERSITY Division of Atomic Physics Department of Physics P. O Box 118 SE-221 00 Lund, Sweden	DOCTORAL DISSERTATION Date of issue 2020-08-25
Author(s) Carl Ekström	Sponsoring organization

Title and subtitle

Acoustic, Thermal and Non-thermal Dynamics in Condensed Matter Studied by Time-Resolved X-ray Diffraction

Abstract

The method of using short laser and X-ray pulses to investigate dynamics in materials (pump-probe) has been used for several decades. This thesis presents work that was carried out using these sources of light to reveal acoustic, thermal and non-thermal dynamics. The dynamics were induced in the samples by depositing energy with a pulsed laser, and probed with X-ray diffraction. The recent increase in the availability of ultrashort X-ray source facilities, such as the FemtoMAX beamline at the MAX IV laboratory, has made it possible to carry out increasing numbers of experiments with femtosecond time resolution. The main part of the experiments were carried out on femto- and picosecond timescales.

When an intense laser pulse impinges on a semiconductor the large number of electrons excited can result in melting of the material within a time much shorter than the time taken to melt the material thermally. At lower intensities and on longer timescales the heat will instead lead to thermally expansion of the material, generating acoustic waves that propagate into the material. Part of the work presented in this thesis involves experiments on atomic disordering during non-thermal melting and modification of the propagating acoustic waves in the semiconductor indium antimonide (InSb). The other material studied in this work was graphite.

The relaxation of the material thermally expanded by laser irradiation was studied to measure the thermal cross-plane conductivity of a graphite film. An accurate measurement of the film thickness was carried out at the same time. An intense laser pulse was also used to generate large amplitude pressure waves in graphite, which may provide a means of driving a direct phase transition from graphite to diamond.

To summarize, this thesis presents experimental work and new findings that contribute to our understanding of the physics in semiconductors, and to the development and properties of materials such as thin films and nano diamonds formed in graphite.

Key words

X-ray diffraction, Time-resolved, Ultrafast, Non-thermal melting, Thermal conductivity, Pressure wave, Opto-acoustic transducer

Classification system and/or index terms (if any)

Supplementary bibliographical information	Language English
ISSN and key title 0281-2762, Lund Reports on Atomic Physics, LRAP 566	ISBN 978-91-7895-508-4 (print) 978-91-7895-509-1 (pdf)
Recipient´s notes	Number of pages 150 Price
	Security classification

Distribution by (name and address)

Signature  Date 2020-08-10

Acoustic, Thermal and Non-thermal Dynamics in Condensed Matter Studied by Time-Resolved X-ray Diffraction

Carl Ekström

LUND
UNIVERSITY

Department of Physics
Division of Atomic Physics
Faculty of Engineering
Lund University
P. O Box 118
SE-221 00 LUND
SWEDEN

ISBN: 978-91-7895-508-4 (print)
ISBN: 978-91-7895-509-1 (pdf)

ISSN: 0281-2762
Lund Reports on Atomic Physics, LRAP 566 (2020)
Printed in Sweden by Media-Tryck, Lund University, Lund 2020

Media-Tryck is a Nordic Swan Ecolabel certified provider of printed material. Read more about our environmental work at www.mediatryck.lu.se
MADE IN SWEDEN

Contents

Abstract

The method of using short laser and X-ray pulses to investigate dynamics in materials (pump-probe) has been used for several decades. This thesis presents work that was carried out using these sources of light to reveal acoustic, thermal and non-thermal dynamics. The dynamics were induced in the samples by depositing energy with a pulsed laser, and probed with X-ray diffraction. The recent increase in the availability of ultrashort X-ray source facilities, such as the FemtoMAX beamline at the MAX IV laboratory, has made it possible to carry out increasing numbers of experiments with femtosecond time resolution. The main part of the experiments were carried out on femto- and picosecond timescales.

When an intense laser pulse impinges on a semiconductor the large number of electrons excited can result in melting of the material within a time much shorter than the time taken to melt the material thermally. At lower intensities and on longer timescales the heat will instead lead to thermally expansion of the material, generating acoustic waves that propagate into the material. Part of the work presented in this thesis involves experiments on atomic disordering during non-thermal melting and modification of the propagating acoustic waves in the semiconductor indium antimonide (InSb). The other material studied in this work was graphite.

The relaxation of the material thermally expanded by laser irradiation was studied to measure the thermal cross-plane conductivity of a graphite film. An accurate measurement of the film thickness was carried out at the same time. An intense laser pulse was also used to generate large amplitude pressure waves in graphite, which may provide a means of driving a direct phase transition from graphite to diamond.

To summarize, this thesis presents experimental work and new findings that contribute to our understanding of the physics in semiconductors, and to the development and properties of materials such as thin films and nano diamonds formed in graphite.

List of publications

This thesis is based on the following publications, which are referred to in the text by their roman numerals:

I **Communication: Demonstration of a 20 ps X-ray switch based on a photoacoustic transducer**

A. Jarnac, Xiaocui Wang, Å. U. J. Bengtsson, **J. C. Ekström**, H. Enquist, A. Jurgilaitis, D. Kroon, A. I. H. Persson, V.-T. Pham, C. M. Tu, and J. Larsson.
Structural Dynamics 4, 051102 (2017)

II **FemtoMAX - an X-ray beamline for structural dynamics at the short-pulse facility of MAX IV**

H. Enquist, A. Jurgilaitis, A. Jarnac, Å. U. J. Bengtsson, M. Burza, F. Curbis, C. Disch, **J. C. Ekström**, M. Harb, L. Isaksson, M. Kotur, D. Kroon, F. Lindau, E. Mansten, J. Nygaard, A. I. H. Persson, V. T. Pham, M. Rissi, S. Thorin, C.-M. Tu, E. Wallén, X. Wang, S. Werin and J. Larsson.
J. Synchrotron Rad. 25, 570-579 (2018)

III **Generation of a large compressive strain wave in graphite by ultrashort-pulse laser irradiation**

Xiaocui Wang, A. Jarnac, **J. C. Ekström**, Å. U. J. Bengtsson, F. Dorchies, H. Enquist, A. Jurgilaitis, M. N. Pedersen, C.-M. Tu, M. Wulff, and J. Larsson.
Structural Dynamics 6, 024501 (2019)

IV **Role of thermal equilibrium dynamics in atomic motion during nonthermal laser-induced melting**

Xiaocui Wang, **J. C. Ekström**, Å. U. J. Bengtsson, A. Jarnac, A. Jurgilaitis, Van-Thai Pham, D. Kroon, H. Enquist, and J. Larsson.
Phys. Rev. Letters 124, 105701 (2020)

V **Repetitive non-thermal melting as a timing monitor for femtosecond pump/probe X-ray experiments**

Å. U. J. Bengtsson, **J. C. Ekström**, Xiaocui Wang, A. Jurgilaitis, Van-Thai Pham, D. Kroon, and J. Larsson.
Submitted (2020)

VI **Acoustic response and cross-plane thermal conductivity of a thin graphite film measured with time-resolved X-ray diffraction**

J. C. Ekström, Å. U. J. Bengtsson, S. Checchia, H. Coudert-Alteirac, A. Jurgilaitis, D. Kroon, A. N. Obraztsov, V.-T. Pham, C. C. Popescu, A. Stenquist, and J. Larsson.
Submitted (2020)

Other relevant publications not included in this thesis

High-resolution macromolecular crystallography at the FemtoMAX beamline with time-over-threshold photon detection

M. Jensen, V. Ahlberg Gagnér, J. Cabello Sánchez, Å. U. J. Bengtsson, **J. C. Ekström**, T. Björg Úlfarsdóttir, M-J Garcia-Bonete, A. Jurgilaitis, D. Kroon, V-T Pham, S. Checcia, H. Coudert-Alteirac, S. Schewa, M. Rössle, H. Rodilla, J. Stake, V. Zhaunerchyk, J. Larsson and G. Katona.
Submitted (2020)

Stabilizing a high-pressure phase in InSb at ambient conditions with a laser-driven pressure pulse

A. Jarnac, Xiaocui Wang, Å. U. J. Bengtsson, M. Burza, **J. C. Ekström**, H. Enquist, A. Jurgilaitis, N. Kretzschmar, A. I. H. Persson, C. M. Tu, M. Wulff, F. Dorchies, and J. Larsson.
arXiv:1712.05370 [cond-mat.mtrl-sci] (2017)

Popular Scientific Summary

Light consists of electromagnetic waves, and is usually described by its wavelength. The wavelength of electromagnetic waves extends over a wide range, from several meters (radio waves) down to dimensions much smaller than the size of an atom. In the short-wavelength part of the spectrum, where the wavelength is on the order of the distance between the atomic planes in a crystal ($\sim 10^{-10}m$), the radiation is called X-rays. At these short wavelengths, diffraction occur from atomic planes making X-ray radiation a perfect tool for studying the structure of crystalline materials. The method used in the studies described in this thesis is called time-resolved X-ray diffraction. Short pulses of X-ray radiation are used to study the rapid changes in a material after excitation by a laser pulse. The changes over time can then be studied by varying the arrival time of the X-ray pulse relative to the laser pulse. The timescale studied was between $10^{-9}s$ and $10^{-15}s$. Ultrashort laser pulses with pulse durations on the order of $\sim 10^{-15}s$ were used in the studies presented in this thesis.

Two different materials were studied, graphite and indium antimonide (InSb). The thermal conductivity and the acoustic response of a thin film of graphite was studied after heat deposition by a laser pulse. In another experiment, high-pressure waves were generated in a sample of natural graphite by an intense laser pulse. The pressure generated was capable of transforming the material from graphite to diamond. In the studies on InSb, acoustic phonons and non-thermal melting were studied. In the first experiment, acoustic strain pulses were generated and modified in InSb to switch X-ray reflection efficiency from the sample. This was done by modifying the acoustic phonon spectrum in order to produce short X-ray pulses. In the other kind of experiment non-thermal melting was studied, which is a much faster process than normal thermal melting, and happens before any material is heated.

Populärvetenskaplig sammanfattning

I arbetet som presenteras i den här avhandlingen så används ljus för att undersöka materia. Ljus är elektromagnetiska vågor som utbreder sig med ljusets hastighet (299792458 m/s i vakuum). Egenskaper hos ljus beskrivs av dess våglängd. Våglängden för elektromagnetiska vågor kan variera mellan att vara flera meter, så kallade radiovågor, till att vara extremt korta. I det kortare spektrumet av våglängder, i storleksordningen av avstånd mellan atomer ordnade i en kristallstruktur ($\sim 10^{-10}m$), så kallas vågorna för Röntgenstrålning. I arbetet som den här avhandlingen baseras på så används väldigt korta pulser av Röntgenstrålning för att i tid följa hur olika materials strukturer förändras. Själva strukturförändringarna initieras av korta laserpulser. Laserpulserna som används är väldigt korta och har en varaktighet som bara är en ytterst liten del av en sekund, endast i storleksordningen $\sim 10^{-15}s$. I jämförelse så är det ungefär lika stor skillnad som att jämföra en dag på jorden med universums ålder. Dessa korta pulser av ljus behövs för att kunna studera ultrasnabba fenomen på atomnivå eftersom det inte finns kameror på marknaden som är tillräckligt snabba för att fånga dessa ögonblick.

Efter att en laser och en Röntgenpuls har träffat materialet som undersöks så fångas ögonblicksbilden av Röntgenpulsen upp av en detektor. Genom att skjuta flera laser- och Röntgenpulser som varierar i tid mellan varandra så kan ögonblicksbilder av dynamiken i ett material fångas upp. Principen är densamma som att göra rörlig film med stillbilder. I detta fall så fungerar laserpulsen som blixten och Röntgenpulsen som kamerans slutare.

I den här avhandlingen har egenskaper hos två olika material studerats, grafit och indiumantimonid (InSb). I grafit så har värmeledningen i en tunn grafitfilm med nanometerstor tjocklek studerats, samt hur en intensiv laserpuls kan användas för att generera kraftiga tryckvågor i naturlig grafit. Studierna av indiumantimonid har handlat om hur man kan använda en laserpuls för att akustiskt modifiera reflektionen av röntgenpulsen från materialet till att bli kortare i tid. Ett annat fenomen som har studerats i samma material är icke-termisk smältning, som till skillnad från konventionell termisk smältning uppstår vid intensiv laserstrålning och har ett tidsförlopp som är betydligt kortare än den tid det tar för att termiskt smälta materialet.

Acknowledgements

Many people have contributed to the work presented in this thesis and it would not have been completed without their help. I would like to thank everyone involved, but some deserve my special thanks.

Firstly, I would like to thank my supervisor, Prof. Jörgen Larsson for giving me the opportunity to work in the Ultrafast X-ray Science Group, for his support, and for teaching me to think in a critical way. I would also like to thank my co-supervisor, Dr. Henrik Enquist, for always making time to answer many questions, and also for help with the simulations.

I would also like to thank everyone at the FemtoMAX beamline for their help and support in carrying out the experiments. Andrius, thank you for teaching me to use the beamline, to prepare samples and for your valuable feedback. Thai, thank you for helping me with problems with beamline, and for writing scripts to collect the data. David, thank you for maintaining the laser so that it always worked perfectly. Stefano, thank you for your useful comments during beamtime, and Hélène for help in maintaining the laser when David was on parental leave.

I would also like to thank all previous and present colleagues in the Ultrafast X-ray Science Group. Xiaocui, you helped me in many situations, and were always very patient with me. I admire your ambition and skills, both in research and cooking. Amélie and Anna, for all the support you gave me, especially when I started in the group. Åsa, for spending many late nights with me collecting data. I would also like to thank Chien-Ming, Amit, Armand, Eric and Rebecca for creating such a pleasant environment and for interesting discussions.

I also would like to express my gratitude to everyone at the Division of Atomic Physics: to Anne, for always helping me out with administrative things, Åke, for his help with software and computers, and Jakob for helping me with financial matters. Thanks also goes to Peter, Maher, Cosmin and Axel.

Thanks goes also to the Student Pyrotechnic Association of Lund, *LundaPyrot*, for making my worries explode in the sky in colorful bursts. Finally, I express my deepest thanks to my family and all my friends, especially my sisters Madeleine and Sofie, for always supporting me, and to Yoshie for always being there for me.

Part I

Overview

Chapter 1

Introduction

Since the discovery by Wilhelm Röntgen in 1895, X-rays have been used extensively in both medical and scientific applications. The discovery of X-ray diffraction from crystals [1] made X-rays a very important tool in the investigation of atomic and molecular structures, and has been a driving force in the development of powerful X-ray sources. The number of studies of ultrafast phenomena in crystalline structures using X-ray diffraction has increased in recent decades due to the development of lasers and X-ray facilities that can produce ultrashort pulses. Such short X-ray pulses enable "molecular movies" to be captured as phase transitions occur. Extremely short femtosecond laser pulses, which are on the same order as atomic motion, are used to induce effects in the materials to be studied. In the work presented in this thesis atomic dynamics was studied on the timescale from hundreds of femtoseconds to a few nanoseconds, following excitation by an ultrashort laser pulse. The majority of the experiments has been a part of the commissioning activities at the FemtoMAX beamline at the MAX IV laboratory, making the beamline available for user experiments.

The pump-probe concept is presented in Chapter 2, where the use of amplified laser pulses is presented and methods of converting these pulses into other wavelengths are presented. The basics of X-ray diffraction is presented in Chapter 3. First the general scattering equations are presented followed by the basic crystal structures and geometries used in these experiments. Chapter 4 describes the dynamics probed by X-ray diffraction in this work. This chapter starts with an introduction to strain generation, which is essential in these experiments, then describes the probing of acoustic phonons as well as the Debye-Waller effect. Chapter 5 provides an introduction to non-thermal melting of semiconductors and the inertial model, which was used to describe this phenomenon. This chapter also describes the principle of the X-ray geometry used to carry out the experiments. The generation and detection of large compressive strains in natural graphite and measurements of thermal conductivity in thin films of graphite are presented in Chapter 6. This chapter also describes the simulations performed in this work. Chapter 7 presents the basic insertion devices of

a synchrotron radiation facility. A brief description of the FemtoMAX beamline at the MAX IV laboratory is also presented. Discussion and conclusions from the experimental work are presented in Chapter 8, while Chapter 9 summarizes the findings and presents an outlook on future work.

Chapter 2

Pump Sources

In the work described in this thesis, short laser pulses of near infrared radiation were used. Additionally, pump sources providing THz radiation were developed at the FemtoMAX beamline.

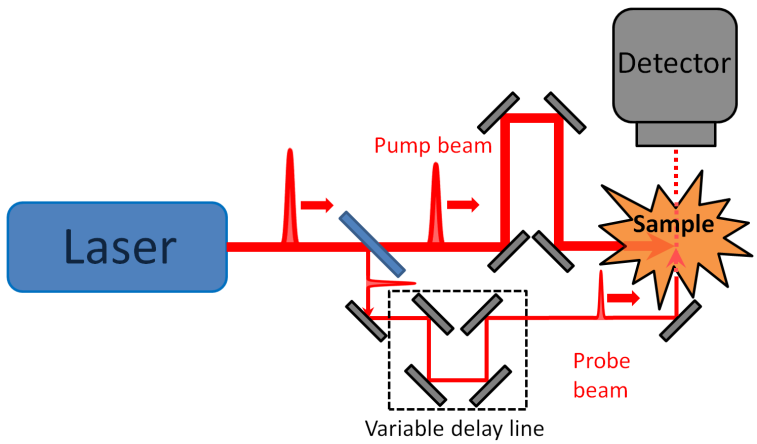

Figure 2.1: Illustration of a typical pump-probe setup. A pulsed laser beam is divided into a pump beam and a probe beam. The travel time of the probe pulse is varied using a delay line.

In ultrafast dynamics, such as atomic or molecular motion and displacements in a material, the effects occur faster than can be resolved using conventional electronic circuits and detectors. The pump-probe technique can be employed to solve this problem. An electromagnetic pulse (the pump) deposits energy that changes the properties of a material. The properties can then be followed in time by additional pulses (the probe) with varying time delays relative to the pump pulse. The pump and probe pulses usually have different properties to match the requirements of pump pulse energy deposition in the material, and

probe pulse characteristics of the material. For example, X-rays are suitable when probing atomic crystal structures, while optical pulses are used to probe surface properties, such as reflection and transmission. The principle of a time-resolved pump-probe experiment is illustrated in Figure 2.1.

2.1 Laser-induced non-linear responses and optical parametric amplifier

The pump sources used in this work were based on the amplification of pulses from a Ti:sapphire laser. Amplified ultrafast optical pulses at a central wavelength of 800 nm that can deliver several mJ of energy were used. The principle of generating short intense laser pulses is based on the method of chirped pulse amplification [2]. This amplification process makes it possible to amplify and compress a laser pulse in time without damaging the optics in the amplification process. The amplified laser pulse can be used directly in experiments as a pump source, or it can be used to further amplify or generate other light sources in optically non-linear materials.

2.1.1 Optically non-linear materials and three-wave mixing

Amplified laser pulses are necessary to induce strong optical ultrafast non-linear responses that can be used to generate additional light. In a linear dielectric material the induced polarization density, P, from an optical electric field E is given by [3]:

$$P = \epsilon_0 \chi E \tag{2.1}$$

where ϵ_0 and χ are the permittivity in free space and the material susceptibility, respectively. In a non-linear material the polarization density can be expressed by Taylor expansion:

$$P = \epsilon_0 \chi E + 2d_{NL}E^2 + 4\chi^{(3)}E^3 + ... = \epsilon_0 \chi E + P_{NL} + 4\chi^{(3)}E^3 + ... \tag{2.2}$$

where $P_{NL} = 2d_{NL}E^2$ is the second-order non-linear polarization density, and d_{NL} is the second-order non-linear coefficient that describes the strength of the second-order non-linear response of the material. If the incident electric field consists of two angular frequencies, $E = E(\omega_1) + E(\omega_2)$, the resulting second-order polarization density will have components that are combinations of the sum and difference of the two frequencies ω_1 and ω_2. The polarization density P_{NL}, will then itself act as a source of light that will emit at the frequencies according to the non-linear wave equation [3]:

$$\nabla^2 E - \frac{1}{c^2}\frac{\partial^2 E}{\partial t^2} = -\mu_0 \frac{\partial^2 P_{NL}}{\partial t^2} \tag{2.3}$$

where c and μ_0 are the speed of light in the material and the permeability in free space, respectively. To ensure efficient generation of light, it is important to match the phase of the propagating and generated light inside the material. The phase matching condition for two light sources with wave vectors $\vec{k_1}$ and $\vec{k_2}$ that radiates light with wave vector $\vec{k_3}$ can then be written:

$$\vec{k_1} + \vec{k_2} = \vec{k_3} \tag{2.4}$$

2.1.2 Optical parametric amplification

Incident light with angular frequency ω_1 and a second wave from an intense laser with angular frequency ω_3 can be phase matched to amplify the first wave in a non-linear crystal. This process is called optical parametric amplification (OPA) and is used to amplify tunable light pulses. In the amplifying process residual light with angular frequency ω_2 is also generated and is called the idler.

It has been suggested in the research group that an optical parametric amplifier could be used as a pump source at infrared wavelengths for non-thermal melting experiments as less heat is deposited. This would finally lead to a non-thermally molten material without any thermal melting. However, OPA excitation as a pump source for this type of experiment had to be abandoned due to problems in matching the pump and probing depths.

2.2 Portable laser-pumped THz sources

Wave mixing in non-linear crystals such as zinc telluride (ZnTe) and lithium niobate ($LiNbO_3$) can be used to enhance the generation of difference frequencies between the spectral components in a laser pulse, and will result in single-cycle THz pulses [4]. A typical laser pulse has a spectral width on the order of $\sim 10^{12} Hz$, which will induce a polarization density at THz frequencies, as described in Section 2.1.1. To be able to combine the THz light generated into a single-cycle pulse, it is important that the group velocity of the laser pulse, c_{gr}, is the same as the speed of light at THz frequencies, c_{THz}, in the material. Figure 2.2 illustrates THz generation in crystals of ZnTe and $LiNbO_3$, commonly used for THz generation from laser pulses.

In ZnTe the velocities of a laser pulse centered at a wavelength of 800 nm and THz light around 1 THz are collinearly matched as $c_{gr} \approx c_{THz}$. This is not the case in the $LiNbO_3$ crystal. The slower generated THz light will lag behind the optical pulse, and the THz phase front will be tilted. To solve this problem it is necessary to tilt the laser pulsefront by this tilting angle to combine the THz light in phase. The result is an intense single-cycle THz pulse that propagates in the direction of this tilting angle. The efficiency of THz generation depends on the non-linear coefficient d_{NL}. Due to the anisotropy of the crystals, it is necessary to take the polarization and direction of the pump laser in the crystal into account in directions where the non-linear coefficient is large.

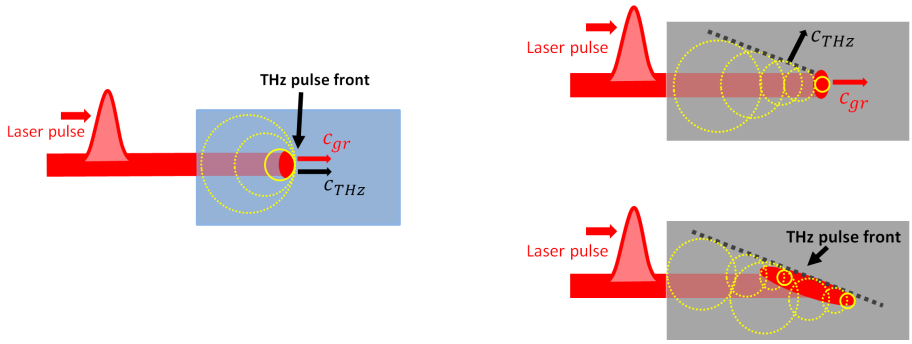

(a) (b)

Figure 2.2: Comparison of THz generation in (a) ZnTe and (b) $LiNbO_3$. In ZnTe the generated THz light adds up in phase to a pulse front. In $LiNbO_3$ the laser pulse front must to be tilted to efficiently combine the THz light into a single pulse. THz generation in the $LiNbO_3$ crystal is shown without and with pulse front tilting. The solid yellow circles represent THz sources at the pulse front, and the dotted yellow circles previously generated THz light.

2.2.1 Organic crystals

Organic crystals can also be used to generate THz pulses. These crystals have extremely large d_{NL}. The main advantages of these crystals are that collinear phase matching can be achieved and the conversion efficiency is higher than in most non-organic crystals. Examples of such crystals are N-benzyl-2-methyl-4-nitroaniline (BNA) [5] and 4-N, N-dimethylamino-4'-N'-methyl-stilbazoliumtoyslate (DAST) [6]. BNA can be pumped with amplified laser pulses at 800 nm while DAST must be pumped by longer wavelengths (1200-1500 nm) to ensure phase matching and to avoid absorption [7]. The longer wavelengths can be achieved through OPA. In many cases it is favorable to use BNA since the highly intense laser pulses from a Ti:sapphire amplifier can be used directly without any optical conversion.

2.3 Probe sources

In the pump-probe setup illustrated in Figure 2.1, a laser is used as a probe source. However, many different probe sources can be employed in ultrafast experiments, as described below.

2.3.1 Laser-based probing

Due to their short duration, pulses from a pulsed laser can be used as a probe source, for example, to measure the transient reflection and absorption at a sample surface [8] and

for spectroscopic measurements [9]. A novel way of probing ultrafast responses with laser spectroscopy is by time-resolved Raman microscopy. A laser pump-Raman probe station has recently been built at the Division of Atomic Physics at Lund University to measure the coherence time of phonons in diamond [10]. However, laser-based probing methods are usually limited to use in probing the reflection, transmission, and absorption of a sample, and cannot probe the dynamics or changes in the atomic structure. To be able to probe atomic structures other sources, such as X-rays and electrons, must be used.

2.3.2 X-rays

X-rays were used as the probe source in the work presented in this thesis. X-rays can be used to measure reflectivity, absorption, and transmission, as in the case of a laser-based source. However, an important property of X-rays is their diffraction from crystallographic planes. This property makes it possible to directly probe the dynamics of the material. X-ray diffraction are further discussed in Chapter 3, and X-ray sources in Chapter 7.

2.3.3 Electron diffraction

Accelerated electrons can be used as a probe source as a complement to X-rays. Diffraction occurs due to the wave nature of electrons [11], and thus diffraction patterns can be acquired. Wavelengths that are much shorter than those that can be produced at synchrotron facilities can be achieved by accelerating electrons to several MeV. Our research group has previously carried out experiments using time-resolved electron diffraction [12].

Chapter 3

X-ray Diffraction

The X-ray radiation used in this work was produced at synchrotron facilities, at wavelengths between ~ 0.4 and 6 nm. In X-ray science, the unit most frequently used to describe light is energy, expressed in eV. The relation between wavelength and energy in eV is given by the relation:

$$E = \frac{hc}{e\lambda} \tag{3.1}$$

where h, c, e and λ are Planck's constant, speed of light, elementary charge and wavelength respectively. X-ray wavelengths are on the order of the distance between atomic planes in crystals, which makes X-rays suitable as a tool to investigate atomic motion and structural dynamics in crystal structures by diffraction. Diffraction arises from light scattered by the electrons in the atoms of the crystal structure. The scattering of X-rays by electrons can either be elastic (Thomson scattering) or modified (Compton scattering). In elastic scattering the energy of the photons is preserved, while in the modified scattering the energy of the photons is reduced. Elastic scattering is dominant in X-ray diffraction experiments, and the modified scattering was thus disregarded in this work.

3.1 X-ray scattering

3.1.1 X-ray scattering from a single electron

A free electron accelerated by an oscillating electric field, in this case X-ray radiation, will emit electromagnetic radiation as it oscillates around an equilibrium position. At a point of observation at a given distance from the electron, the observable scattered intensity is given by Equation [13]:

$$I = I_0 \frac{e^4}{m^2 c^4 R^2} \left(\frac{1 + \cos^2 \phi}{2} \right) \tag{3.2}$$

where I_0 is the intensity of the incident oscillating field, e is the elementary charge, m is the electron mass, c the speed of light, R the distance between the charge and the point of observation and ϕ the angle between the direction of observation and the oscillating charge.

3.1.2 X-ray scattering from an atom

In contrast to a free electron the intensity of the radiation scattered by an atom includes contributions from all the electrons in the electron cloud surrounding the nucleus. An important quantity in X-ray diffraction is the atomic scattering factor, f, which describes the amplitude of scattered light per atom. The expression for the atomic scattering factor is [13]:

$$f(\vec{Q}) = \int_0^\infty \rho(\vec{r}) e^{i\vec{Q}\cdot\vec{r}} d\vec{r} \tag{3.3}$$

where $\rho(\vec{r})$ is the radial density distribution of electrons, $\vec{Q}$ the scattering vector and $\vec{r}$ the position vector. Scattering factors for most materials can be found in tables for X-ray crystallography [14].

3.1.3 X-ray scattering from a crystal

In a crystalline structure, the atoms are arranged in a specific repeating order. The smallest unique unit in this structure is called the unit cell. The scattering from a unit cell is a result of the interference of the light scattered from all the atoms in the unit cell, which depends on the position x_n, y_n, z_n, of each atom, n, with a scattering factor, f_n, within the unit cell. This is described by the sum of the atomic scattering factors f_n, and is called the structure factor, F_{hkl}:

$$F_{hkl} = \sum_n f_n e^{2\pi i(hx_n + ky_n + lz_n)} \tag{3.4}$$

The integers h, k, and l are called the Miller indices, and define the atomic planes in the crystal. The square of the structure factor is proportional to the intensity of scattered radiation from the crystal. For the two materials studied in this thesis, InSb and graphite, which have zinc-blende cubic and hexagonal structures respectively, the structure factors can be derived from the atomic positions in their respective unit cell. Due to this dependence on the atomic positions, there are cases where the structure factor is zero and no reflection is observed. These reflections are called forbidden reflections, and occur in InSb when the Miller indices includes both even and odd integers. For graphite, all reflections with $l =$ odd will be forbidden.

3.1.4 X-ray scattering from planes of atoms and Bragg's law

In general, the atomic planes in a crystal can be illustrated as a chain of atoms which may all scatter radiation in phase during irradiation, as illustrated in Figure 3.1.

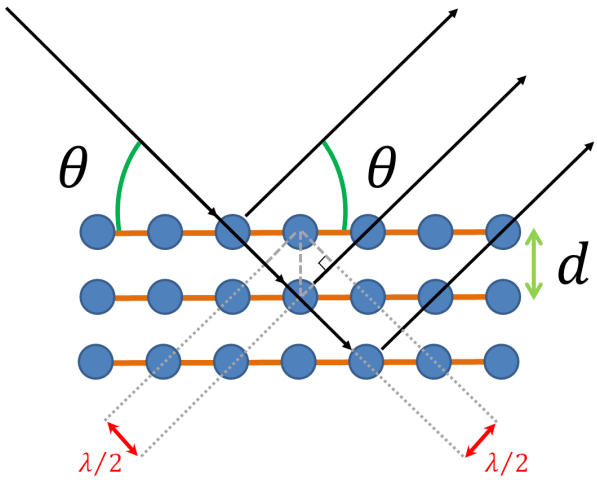

Figure 3.1: Illustration of Bragg's law. The blue circles denote the atomic planes with interplanar spacing d.

The atomic planes are separated by the interplanar spacing, d. When incident X-rays of a specific energy propagate through the atomic layers the electrons will scatter light with the same wavelength as the incident radiation. If the angle of incidence is θ, then the X-ray radiation scattered from the upper and lower atomic planes will be in phase when the path difference of the light, $2d\sin\theta$, is an integer multiple, N, of the wavelength, λ. This condition is known as Bragg's law [1], and is expressed as in equation 3.5.

$$2d\sin\theta = N\lambda \tag{3.5}$$

3.2 Crystal structures

3.2.1 Crystallographic planes and Miller indices

As mentioned above, the atoms in a crystal structure will form crystallographic planes that can be defined using the Miller indices. If the crystallographic axes are a_1, a_2 and a_3, then the crystallographic set of planes hkl are defined as the planes going through the origin and $a_1/h, a_2/k$ and a_3/l. The crystallographic axes and the planes with Miller indices (010) and (002) are illustrated in Figure 3.2.

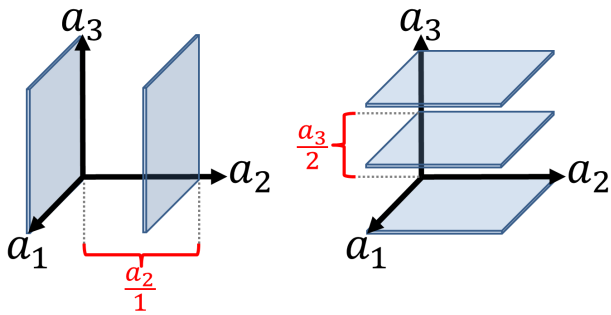

Figure 3.2: Illustration of crystallographic planes with Miller indices (010) and (002). The red bracket marks the distance $a_1/1$ and $a_3/2$ on each figure.

3.2.2 The reciprocal vectors and the scattering vector

A useful way of treating the crystallographic planes in X-ray diffraction is by defining a set of reciprocal vectors, $\vec{b_1}, \vec{b_2}$, and $\vec{b_3}$, each one perpendicular to two crystallographic axes. The reciprocal vectors are defined as [13]:

$$\vec{b_1} = 2\pi \frac{\vec{a_2} \times \vec{a_3}}{\vec{a_1} \cdot \vec{a_2} \times \vec{a_3}}, \quad \vec{b_2} = 2\pi \frac{\vec{a_3} \times \vec{a_1}}{\vec{a_1} \cdot \vec{a_2} \times \vec{a_3}}, \quad \vec{b_3} = 2\pi \frac{\vec{a_1} \times \vec{a_2}}{\vec{a_1} \cdot \vec{a_2} \times \vec{a_3}} \tag{3.6}$$

The vectors in Equation 3.6 can then be used to define the scattering vector $\vec{Q_{hkl}}$, as the linear combination of the Miller indices and reciprocal vectors:

$$\vec{Q_{hkl}} = h\vec{b_1} + k\vec{b_2} + l\vec{b_3} \tag{3.7}$$

Since the reciprocal vectors are perpendicular to the crystallographic axes that define each crystallographic set of planes (hkl), the scattering vector will be a vector perpendicular to this set of planes. In the left-hand illustration in Figure 3.2, the interplanar spacing is $d_{010} = |\vec{a_2}|$. It then follows that:

$$|\vec{Q_{010}}| = |\vec{b_2}| = 2\pi \frac{|\vec{a_3}||\vec{a_1}|}{|\vec{a_1}||\vec{a_2}||\vec{a_3}|} = \frac{2\pi}{|\vec{a_2}|} = \frac{2\pi}{d_{010}} \tag{3.8}$$

Hence the magnitude of the scattering vector is related to the interplanar spacing as:

$$|\vec{Q_{hkl}}| = \frac{2\pi}{d_{hkl}} \tag{3.9}$$

Bragg's law in vector form

A more general way of expressing Bragg's law is in vector form, where wave vectors represent the incident and scattered X-rays. Since the magnitudes of the incident and scattered X-rays are equal, it can be shown that Equation 3.5 is Equivalent to equation 3.10, where $\vec{k_s}$

and $\vec{k_0}$ are the wave vectors of the scattered and incident X-rays, respectively, θ is the Bragg angle, and $\vec{Q}$ is the scattering vector. Figure 3.3 illustrates Bragg's law in vector form.

$$\vec{k_s} - \vec{k_0} = \vec{Q} \tag{3.10}$$

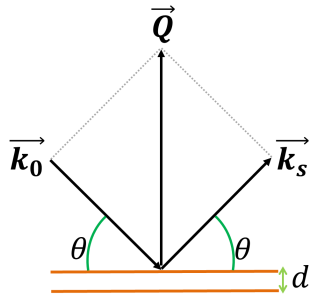

Figure 3.3: Bragg's law in vector form.

3.2.3 Crystals and lattice spacing

The two materials investigated in this work had different structures, and therefore, the interplanar spacing, d_{hkl}, is calculated differently. In a cubic crystal such as InSb all three crystal axes are equally long, $|\vec{a_1}| = |\vec{a_2}| = |\vec{a_3}| = a$, and orthogonal, while in the case of hexagonal crystals, such as graphite, the interplanar spacing depends on the two crystal axes, $a_a = |\vec{a_1}|$ and $a_c = |\vec{a_3}|$. The different crystal structures are illustrated in Figure 3.4.

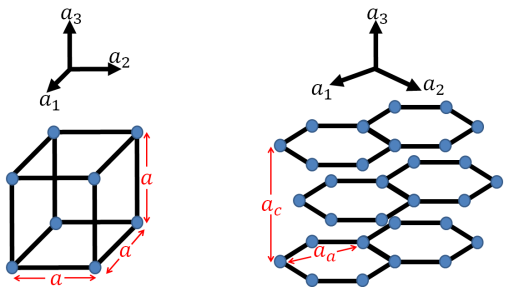

Figure 3.4: Illustration of a simple cubic crystal and a hexagonal crystal.

The relation between the crystal axes and Miller indices gives expressions for the spacing in cubic and hexagonal crystals [13]:

$$\textbf{Cubic: } d_{hkl} = \frac{a}{\sqrt{h^2 + k^2 + l^2}}, \qquad \textbf{Hexagonal: } d_{hkl} = \frac{1}{\sqrt{\frac{4}{3}\left(\frac{h^2+hk+k^2}{a_a^2}\right) + \frac{l^2}{a_c^2}}} \tag{3.11}$$

3.3 Diffraction geometry

3.3.1 Coplanar and non-coplanar geometry

When investigating the geometry of a certain X-ray reflection from a set of planes, two geometries of diffraction, coplanar and non-coplanar, can be distinguished. In the coplanar geometry the incident and scattered wave vectors, $\vec{k_0}$ and $\vec{k_s}$, and the scattering vector, $\vec{Q}$, are in the same plane, which is normal to the crystal surface. All other geometries are called non-coplanar. Figure 3.5 illustrates the two different diffraction geometries.

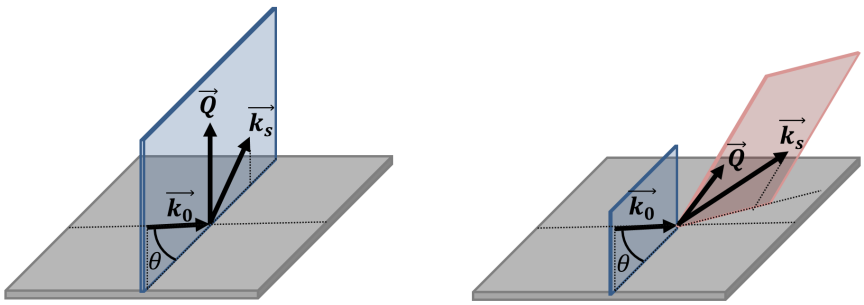

Figure 3.5: Illustration of the coplanar (a) and non-coplanar (b) reflection geometry. In the non-coplanar case the vectors are not in the same plane.

3.3.2 Asymmetric diffraction geometry

In contrast to a symmetric case, illustrated in Figure 3.6 (a), crystals can be cut relative to a set of crystallographic planes so that the orientation of the sample surface and the crystallographic planes will be different. In such cases the diffraction geometry is called asymmetric. The simple case where the Bragg reflection geometry is coplanar is illustrated in Figure 3.6 (b).

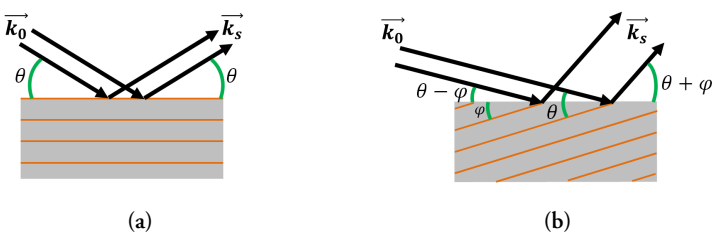

Figure 3.6: Illustration of symmetric (a) and asymmetric (b) diffraction geometry for a coplanar reflection.

According to the Bragg condition illustrated in Figure 3.3, the angles of the incident and scattered wave vectors relative to the crystallographic planes, θ, are equal. This means that the surface is parallel to the crystallographic planes, and hence the incident and exit angles relative to the sample surface are the same. In the asymmetric case, Figure 3.6 (b), the surface and the crystallographic planes are not parallel, but are at an angle φ to the surface. In order to fulfill the Bragg condition in this case, the angle of incidence relative to the surface will be $\theta-\varphi$, and consequently the exit angle must be $\theta+\varphi$. Asymmetric diffraction geometries with a very small angle of incidence have been used previously in experiments to study non-thermally molten layers in InSb [15, 16]. These are usually referred to as grazing incidence X-ray scattering (GIXS) experiments [17].

Probing depth

Using an asymmetric diffraction geometry, as illustrated in Figure 3.6 (b), can be beneficial as the incident X-rays will propagate closer to the sample surface. This will make the experiment more sensitive to probing the surface layers rather than deeper in the material. In most materials, the refractive index for X-rays is less than unity [13]. This must be taken into account when calculating the probing depth, d_p. Refraction will thus take place at the surface, and the angle in the material, θ_2, will increase as a consequence of Snell's law. This will further decrease the probing depth, as illustrated in Figure 3.7.

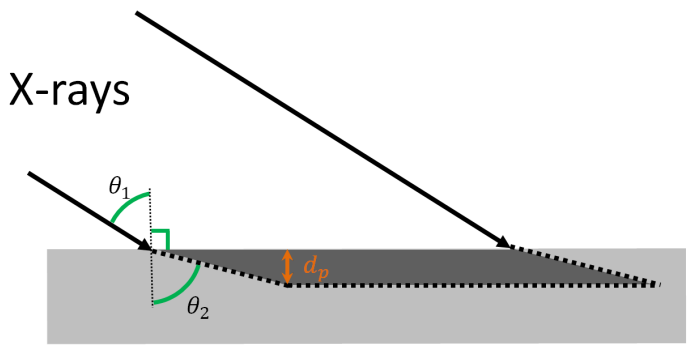

Figure 3.7: Illustration of the probing depth, d_p, at an X-ray incidence angle θ_1. The refractive index of the material is less than unity for X-rays, further reducing the probing depth.

In some laser pump-X-ray probe experiments the probing depth of the X-rays must be matched with the depth of laser excitation. This was the case in the study presented in Paper IV, where only non-thermally molten effects at the sample surface were probed.

Chapter 4

Probing Lattice Dynamics with X-ray Diffraction

Heating a crystal using an ultrafast laser pulse will cause thermal expansion of the material due to the increase in temperature. The crystallographic planes in the rapidly stressed material will be displaced, and is usually referred to as strain. Probing the strain in a material using time-resolved X-ray diffraction, allows acoustic phonons and strain-related properties to be studied.

4.1 Acoustic wave propagation in solids

If we assume a one-dimensional structure, the relation between the absorbed fluence, F, from a laser pulse in a material and the temperature increase, ΔT, at a depth z is given by:

$$\Delta T(z) = \frac{W(z)}{C} = \frac{F}{\zeta C} e^{-z/\zeta} \tag{4.1}$$

where $W(z)$ is the energy density, C the specific heat constant, and ζ the optical absorption depth of the material.

4.1.1 The Thomsen model

A simplified model describing one-dimensional longitudinal strain evolution during ultrafast excitation by a laser pulse has been given by Thomsen *et al.* [18]. In their model, the thermal expansion of the lattice, and thus the stress driving the strain, is assumed to occur instantaneously. The strain at depth z and time t is given by:

$$\eta(z,t) = \frac{F\beta}{\zeta C}\frac{1+\nu}{1-\nu}\left[e^{-z/\zeta}\left(1-\frac{1}{2}e^{-vt/\zeta}\right) - \frac{1}{2}e^{-|z-vt|/\zeta} sgn(z-vt)\right] \tag{4.2}$$

where β is the thermal expansion coefficient, ν the Poisson ratio, and v the speed of sound.

In order to fulfill the initial condition, i.e., no strain has developed, the solution yields two travelling waves and a static part at the surface, which can be identified by the terms in the square brackets in Equation 4.2. As the travelling strain waves propagate, one will immediately be reflected at the surface, and therefore a pulse consisting of negative and positive parts will form that propagate into the material. Equation 4.2 is illustrated in Figure 4.1 as a function of depth. The width of the strain parts depends on the heat deposited in the material by the laser. Equation 4.1 shows an exponential deposition profile and hence the strain will have the same profile. The absorption depth used in the case shown in Figure 4.1 was $\zeta = 100nm$.

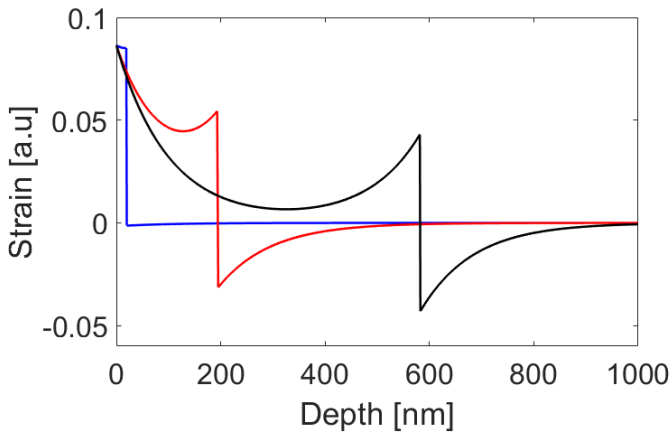

Figure 4.1: Strain development obtained using the Thomsen model at 5 (blue), 50 (red) and 150 (black) ps after laser heat deposition, as a function of depth.

4.1.2 Acoustic reflection and mismatching

Equation 4.2 is valid until the travelling acoustic strain pulse reaches a part of the sample where the acoustic impedance changes. From that point on, acoustic reflections must be considered. Figure 4.1 illustrates the case for a thick sample ($> 1\mu m$). However, for samples with a finite size, the acoustic strain pulse will be reflected from the back surface. When the strain pulse propagates in a film on top of a substrate it will be transmitted into the substrate. The reflection and transmission coefficients, R_η and T_η, depend on the acoustic impedance, Z_i, of the materials, and are given by the following equations [19]:

$$R_\eta = \frac{Z_2 - Z_1}{Z_2 + Z_1}, \quad T_\eta = \frac{B_1}{B_2}\frac{2Z_2}{Z_2 + Z_1}, \quad Z_i = \rho_i v_i \tag{4.3}$$

where ρ_i, v_i and B_i are the density, velocity of sound, and bulk modulus, respectively.

The subscript i refers to the material of propagation ($i = 1$) and transmission ($i = 2$). Propagating and reflecting strain pulses from a boundary are shown in Figure 4.2. In (a) the second material is vacuum ($Z_2 = 0$) and the strain pulse will have the same amplitude but show a phase shift of π. In (b) the acoustic impedance of the second material is higher so no phase shift occurs at the boundary.

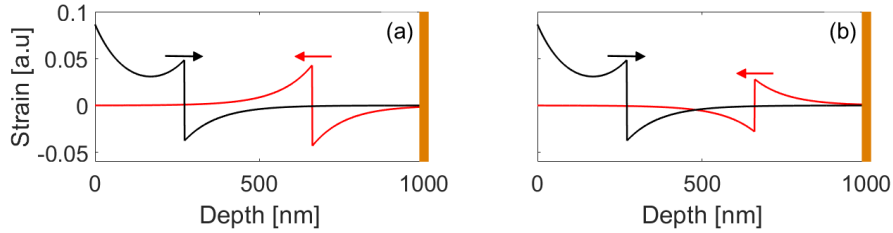

Figure 4.2: Propagating (black) and reflected (red) acoustic strain waves. The boundary is indicated by the solid orange line. The black and red arrows show the direction of propagation of each strain pulse.

Applications

If the acoustic mismatch between the thin film and the substrate is large, the reflections of the strain pulse can be used to determine the thickness of the film. This method was used in the study presented in Paper VI to determine the thickness of the thin film of graphite grown on a nickel substrate. In the study described in Paper I, the acoustic mismatch between a gold film and an InSb substrate was used to transmit strain echoes into the substrate with a periodicity that enhanced or cancelled out specific phonon modes.

4.2 Acoustic phonons

Lattice vibrations can be described by particles that are quantified by their frequency. These particles are called phonons. Phonons are categorized by their vibrational direction relative to their direction of propagation, transversal or longitudinal, and whether they are optical or acoustic [20]. In the work presented here, only longitudinal acoustic phonons were observed, and will be the only kind discussed. From the description of acoustic phonons, the strain induced in a material during ultrafast excitation by a laser pulse can be considered as a superposition of coherent acoustic phonons, and can thus be described to contain a phonon spectrum. The acoustic phonons can be studied by time-resolved X-ray diffraction [21, 22] and be modified by ultrafast laser pulses to enhance or cancel specific frequencies [23, 24, 25, 19].

4.2.1 Scattering condition for acoustic phonons

The Bragg condition, discussed previously in Section 3.2.2 and illustrated in Figure 3.3 is valid for an unperturbed lattice. If a phonon with wave vector $\pm\vec{q}$ exists in the solid, then the wave vectors of the incident and scattered X-rays, $\vec{k_0}$ and $\vec{k_s}$, must be modified in order to fulfill the Bragg condition. With a phonon wave vector the Bragg condition will be as stated in Equation 4.4. Figure 4.3 illustrates the Bragg condition.

$$\vec{k_s} - \vec{k_0} = \vec{Q} \pm \vec{q} \tag{4.4}$$

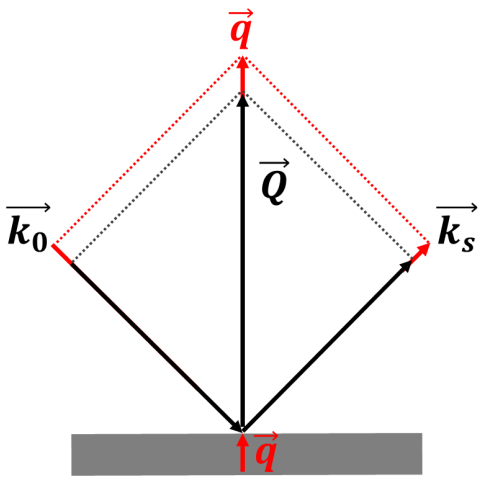

Figure 4.3: Bragg condition for probing acoustic phonons with a wave vector $\vec{q}$.

The condition in Equation 4.4 makes it possible to probe individual acoustic phonons in a solid by detuning the X-ray energy away from the Bragg peak [22].

4.3 The Debye-Waller factor

In a perfect structure with well defined atomic positions, the scattered intensity will be determined as described previously in Chapter 3. However, the atoms in the crystal structure will vibrate, thus having an average kinetic energy depending on the temperature. These vibrations will introduce an uncertainty in the positions of the atoms and decrease the scattered intensity. To take thermal vibrations into account, the diffracted X-ray intensity from a solid material is multiplied by a factor that depends on the average thermal displacement of the atoms. This factor is called the Debye-Waller factor [13]. For a solid material with one kind of atom, the diffracted intensity is given by:

$$I = I_0 e^{-2M}, \quad 2M = 16\pi^2 \langle u^2 \rangle \frac{\sin^2\theta}{\lambda^2} \tag{4.5}$$

where I_0 is the X-ray intensity, θ the Bragg angle and $\langle u^2 \rangle$ is the average of the squared displacements from the equilibrium positions of the atoms in the normal direction of the crystallographic planes.

Chapter 5

Non-thermal Melting of Semiconductors

Melting a solid to form a liquid is usually carried out by resistive heating. This will make the atoms in the solid vibrate until the atomic bonds are broken. Once these bonds are broken, the solid restoring forces disappear and a liquid state is formed. Melting can also be induced by a laser pulse. The energy of the laser pulse is deposited in the electron system, which then thermally equilibrates with the lattice through electron-phonon coupling, and takes place on the timescale of picoseconds [26]. However, an additional non-thermal melting process exists in laser-induced melting [27, 28], in which the bonds are broken directly after laser excitation. The electrons that are excited are the same as those forming the atomic bonds. When these electrons are excited into the conduction band the bonds are broken, and the material turns into a liquid [29]. This melting process is faster than thermal melting, and can occur within a fraction of a picosecond. Figure 5.1 shows the reduction in X-ray intensity due to non-thermal melting of InSb, where it can clearly be seen that the melting time is $< 1ps$.

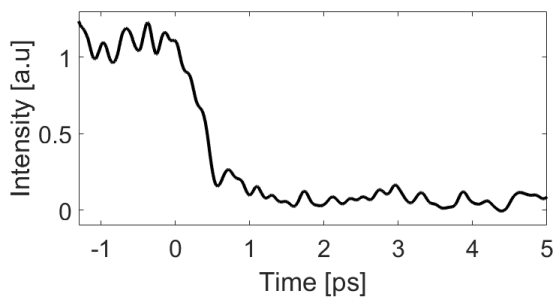

Figure 5.1: Non-thermal melting in InSb. The decrease in the diffracted X-ray intensity takes place on the sub-picosecond timescale.

5.1 The inertial model

Lindenberg *et al.* developed a model to describe the non-thermal melting process [15]. This model assumes that atomic motion in the material after bond breaking will be completely inertial, i.e. the move at their initial thermal velocities, and will thus be dependent on the initial temperature of the material. This model has been found to be valid in InSb within a range of excited carrier densities [16]. A simple illustration of the model is given in Figure 5.2.

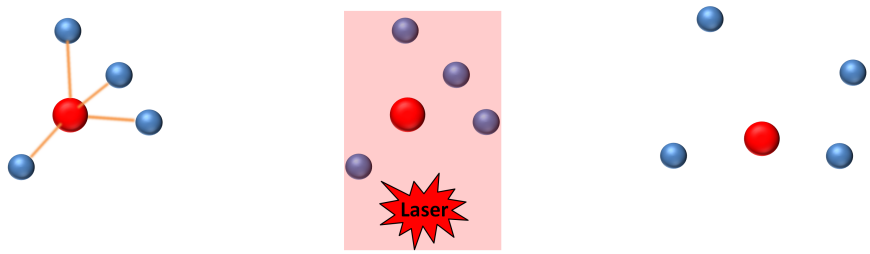

Figure 5.2: Illustration of the inertial model in a simplified case with one In atom (red) and the corresponding four bound Sb atoms (blue). Before laser interaction (a) the atoms are bound and vibrate around their equilibrium positions. Upon laser irradiation (b) the bonds are broken. As the bonds are broken the atoms will become disordered (c) and move at their initial thermal velocities.

5.1.1 Lattice energy and the Debye-Waller formalism

Upon disordering, the description of the average displacement in time of the unbound atoms is similar to the Debye-Waller effect in Equation 4.5. This led Lindenberg *et al.* to a Debye-Waller description of non-thermal melting. If Equation 4.5 is modified to be time dependent with a spatial average of all the excited atoms, then the decrease in the time-dependent normalized diffracted X-ray intensity, I, can be used to describe the inertial model [15]:

$$I(Q_{hkl}, t) = e^{-\frac{Q_{hkl}^2 v_{rms}^2 t^2}{3}} \tag{5.1}$$

where Q_{hkl} is the scattering vector of reflection (hkl), v_{rms} the root mean square of the atomic velocity, and t the time. For a given reflection, Equation 5.1 is then Gaussian with a time constant depending on the scattering vector and the atomic velocity, v_{rms}. The velocity is dependent on temperature and can be calculated from the thermal atomic vibration energy, U:

$$v_{rms} = \sqrt{\frac{U}{M}} \tag{5.2}$$

where M is the average atomic mass. Following the classical description the atomic vibrational energy is then given by:

$$U = 3k_B T \tag{5.3}$$

where k_B and T are the Boltzmann constant and temperature, respectively. In the study described in Paper IV, it was found that the classical description could not adequately describe the experimental findings at lower sample temperatures. This is further discussed in Chapter 8.

5.1.2 Disordering times and atomic velocities

The disordering time in the work presented here is defined as the time taken for the intensity to decrease from 90% to 10% of the initial value. The temperature dependence of the inertial motion will affect the disordering time, as illustrated in Figure 5.3. The inertial model predicts that at lower temperatures the atoms will move with a slower velocity than at room temperatures. As a result, the disordering will be slower at lower temperatures and faster at higher temperatures. The first investigation of the temperature dependence of non-thermal melting in the inertial regime was investigated for the first time, and is described in Paper IV.

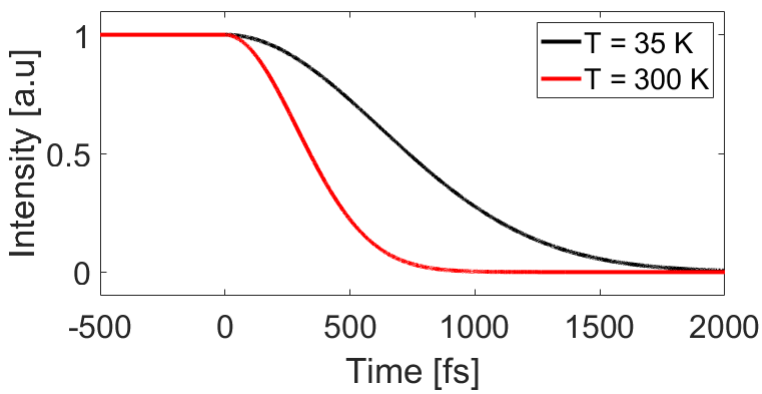

Figure 5.3: Inertial model illustrated for the (111) reflection of InSb at two different sample temperatures. The disordering will be slower at lower sample temperatures (black curve) than at room temperature (red curve).

5.2 Detection of non-thermal melting

To be able to measure fast disordering it is necessary to have good temporal resolution to resolve the decrease in intensity, which takes place on the order of hundreds of femtoseconds. This can be achieved by using a geometry that projects the spatial axis of the sample onto the time axis [30], and is illustrated in Figure 5.4.

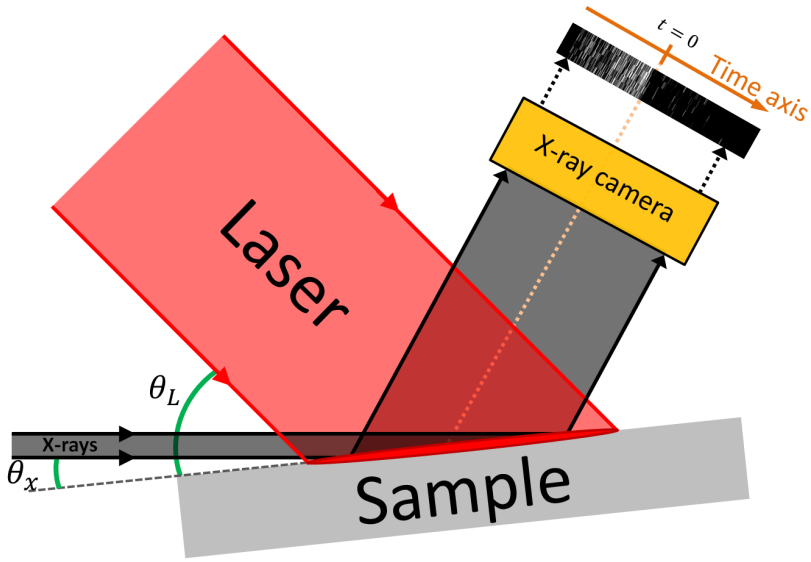

Figure 5.4: Illustration of the spatio-temporal X-ray geometry in a non-thermal melting experiment.

Using a grazing incidence geometry and an asymmetrically cut sample, the spatial coordinates along the laser excitation can be mapped temporally within a time window of a few picoseconds. The grazing incidence geometry is also important to confine the probing depth of the X-rays to the non-thermally molten material, as explained in Section 3.3.2.

5.2.1 Spatio-temporal mapping

When the X-ray and the laser pulses arrive at the sample, they will both make a streak on the sample surface. By changing the relative delay between the two pulses it is possible to make the streaks overlap temporally, so that part of the X-ray reflection contains the spatio-temporal information on the intensity decrease due to the molten material. From the geometry shown in Figure 5.4, the conversion of position on the sample to time is given by:

$$t = \frac{L(\cos\theta_x - \cos\theta_L)}{c} \tag{5.4}$$

where L is the position along the sample, and c the speed of light in vacuum. θ_x and θ_L are the incidence angles of the X-rays and laser relative to the sample surface, respectively.

5.2.2 Incidence angle calibration

Only the upper layers of the sample will be melted non-thermally, which means that the probing depth, and hence the incidence angle of the X-rays must be calibrated. In a grazing incidence geometry this can be done by using the total external reflection of X-rays, in analogy to the total internal reflection in optics. There is external reflection in this geometry since the refractive index for X-rays is less than unity. Good calibration can be achieved by lowering and raising the sample, as illustrated in Figure 5.5 (a), and mapping the position of the external reflection of the X-rays relative to the direct beam position on the detector, (y), while stepwise rotating the angular motor stage. The position on the detector is plotted against the angle of the motor stage and fitting gives a straight line, illustrated in Figure 5.5 (b). The intercept between this straight line and zero position gives the angle of incidence $\theta_{inc} = 0°$.

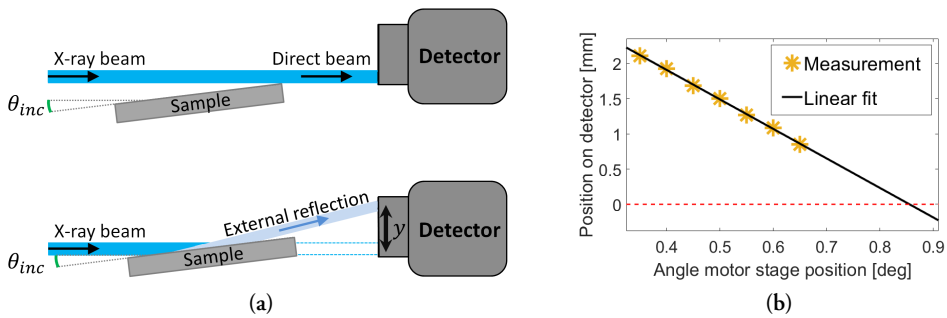

Figure 5.5: Illustration of the calibration of the incidence angle using total external reflection.

Chapter 6

Strain and Heat in Graphite

Graphite consists of stacked layers of carbon atoms ordered in a hexagonal structure with weak van der Waals bonds between the layers, as illustrated in Figure 6.1. Graphite is an interesting material for several reasons. For example, it is an important component in lithium ion batteries [31], and the characterization of single layer graphite (graphene) [32] has become a model material in 2D material research. It is therefore important to characterize the properties of graphite, such as its thermal conductivity, which can differ by several orders of magnitude in the in-plane and cross-plane directions [33]. Studies of graphite during ultrafast laser excitation have also resulted in the generation of nanodiamonds [34, 35]. It has been suggested that the resulting pressure waves rearrange the atomic layers in graphite to form diamond structures. These laser-induced pressure waves can be studied by following the strain waves propagating in graphite.

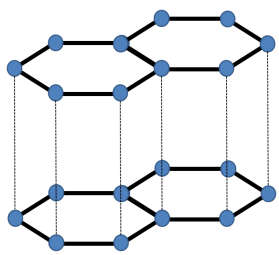

Figure 6.1: Illustration of the hexagonal structure of graphite.

The naturally found structures of carbon are graphite and diamonds. There are several kinds of ordered graphite material in crystalline form, for example, single crystalline natural graphite, and synthetically made materials such as highly oriented pyrolytic graphite (HOPG) and graphene.

6.1 Large compressive strain in natural graphite

Natural diamonds are formed in the mantle of the earth, where the pressure and temperature are extremely high. However, pressure can be induced in graphite by irradiation of the graphite surface using a laser. The pressure is related to the strain in the material, which is defined as the relative displacement of the atomic layers.

Simulations were performed and compared with the strain measured experimentally in X-ray measurements during high-intensity laser irradiation. A hydrodynamic simulation code, ESTHER [36], was used to calculate the change in density between the solid and perturbed material (Paper III). When the experimental values and the simulations were compared, it was seen that the rapid change in density when the material changed from a solid to a liquid state, in the simulations induces the pressure at the surface of the crystal due to the change in volume. In one dimension, this will result in displacement of the atomic layers, i.e. strain in the layers below the melted area. This strain, S, was calculated from the simulations based on the difference in the density of the solid and liquid material using the relation:

$$S(t) = \frac{\rho_0}{\rho(t)} - 1 \tag{6.1}$$

where ρ_0 and $\rho(t)$ are the densities of the solid and perturbed material, respectively. The process is illustrated in Figure 6.2.

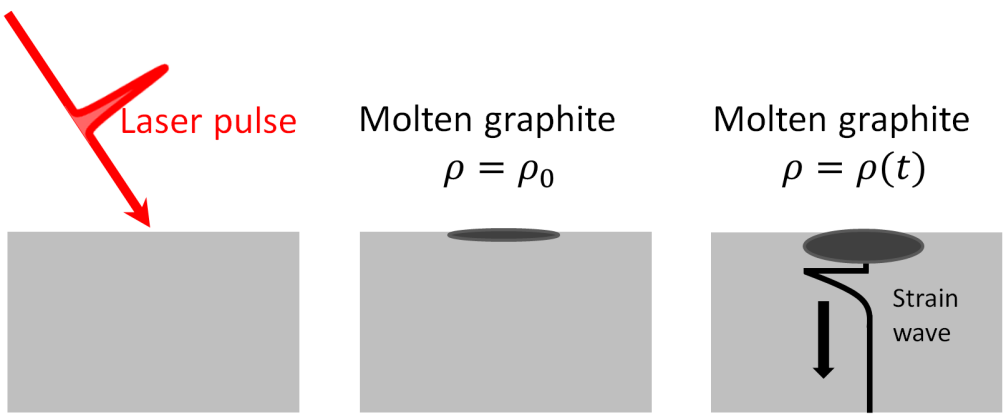

Figure 6.2: Strain wave generation in graphite above the ablation threshold. The laser pulse melts the top layer of a graphite sample. The change in volume at the surface induces stress that displaces the solid material, and resulting in a compressive strain wave.

6.1.1 2D Diffraction simulations

In the experiment described in Paper III, the diffraction spots from the sample were captured by a 2D detector. A diffraction code software that simulates the diffraction pattern on a 2D area detector were used to simulate the effects observed [37]. This code simulates the diffraction pattern for all allowed reflections in a crystalline material. The input parameters required are the experimental parameters such as X-ray energy and geometry, the detector properties, and the crystal structure factors.

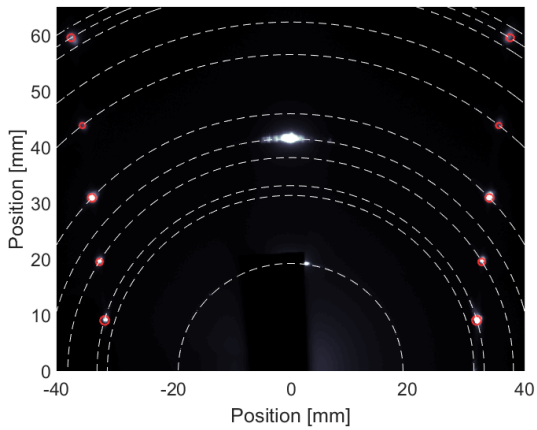

Figure 6.3: X-ray diffraction image of an HOPG sample captured by a 2D detector. The red circles indicate the positions given by the diffraction simulation code. In this illustration only non-coplanar simulated spots are shown. The white dashed circles represent the q values of graphite.

The diffraction spots in Figure 6.3 represent reciprocal space, where the radial distance from the beam center is determined by the scattering vector $\vec{Q_{hkl}}$. The q values, q_{hkl}, can be calculated from the magnitude of the scattering vector (Equation 3.9). For an unperturbed crystal reflection (hkl) the q value is constant. From geometry, the relation between the q value and the Bragg scattering angle can be written:

$$q_{hkl} = \frac{2\pi}{d_{hkl}} = \frac{4\pi}{\lambda} \sin\theta_{hkl} \tag{6.2}$$

where λ is the X-ray wavelength and θ_{hkl} is the Bragg scattering angle. The relation in Equation 6.2 and pre-calculated q values can then be used to calibrate the detector distance D between the sample and detector. This is done by calculating the Bragg scattering angle from the distance r between the direct X-ray beam and the position of the reflection on the detector, as illustrated in Figure 6.4.

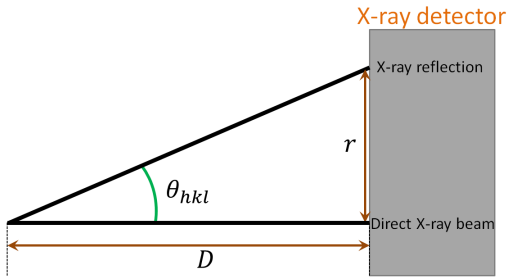

Figure 6.4: Calibration of the sample-detector distance using q-values.

6.1.2 Strain from q values

Strain in crystal layers will change the interplanar spacing, d_{hkl}, which in the simulations changes the position of the reflections, and hence the q values will differ from the static values indicated by the white dashed circles in Figure 6.3. The deviation from the static q values was used to calculate the strain with the equation:

$$S = \frac{q - q'}{q} \tag{6.3}$$

where q and q' are the static and perturbed q values, respectively.

6.2 Thermal conductivity in thin graphite films

Knowledge on the thermal conductivity of graphite has proved to be important in developing efficient lithium ion batteries [31], as well as in other applications, such as the removal of heat from integrated circuits [33]. The thermal conductivity of crystalline graphite is highly anisotropic. In bulk samples, the in-plane thermal conductivity is 2000 W/m-K, whereas the cross-plane value is only 6.8 W/m-K [33]. Due to recent developments in the growth of thin films on substrates, and methods using mechanical exfoliation, the properties of thin films with nanometer thickness can now be studied. In the studies presented in this thesis, the focus was on the cross-plane thermal conductivity.

Heat can be deposited in a graphite film by a laser pulse, and the cross-plane thermal conductivity can be determined by probing relaxation of the strain after heat deposition with time-resolved X-ray diffraction. The first experiment using this method was carried out by Harb *et al.* [38], and this method has been further developed and is used in the present work (Paper VI).

The (002) reflection of graphite was probed, as this is only sensitive to strain in the cross-planar direction, and allows direct measurement of the cross-plane thermal conductivity.

6.2.1 Heat transport in graphite

The main carriers of heat through conduction in solids are electrons and phonons. In the case of graphite which, in contrast to metals, does not have a high concentration of free electrons, the carriers of heat are acoustic phonons [33]. Since the phonons are quantified lattice vibrations, the number of phonon modes will depend on the sample size, the number decreasing as the sample size decreases, thus reducing the thermal conductivity, κ [39]. This is due to the following less heat transport from the phonons. It is therefore important to be able to measure the thickness of the film. This is further discussed in Chapter 8.

6.2.2 Simulations

Strain

Simulations of the strain evolution in a thin film of graphite were carried out using the thermal conduction model in the commercial software COMSOL. A 1-dimensional geometry was implemented for a thin film of graphite on a nickel substrate. To prevent acoustic reflections from the back surface of the substrate influencing the strain profiles, a sufficiently thick substrate, of $100\mu m$, was used. An example of a calculated strain profile for a 33 nm thin graphite film at time $t = 5ps$ after laser excitation is illustrated in Figure 6.5.

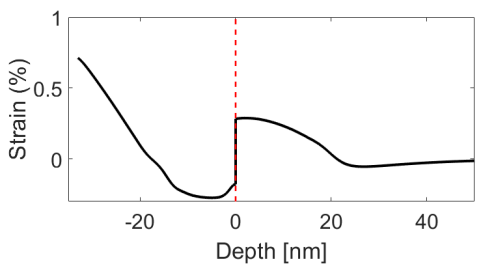

Figure 6.5: Simulation of strain in a thin graphite film at $t = 5ps$. The red dashed line indicates the interface between the film (Depth < 0 nm) and the substrate (Depth > 0 nm).

Heat source

In many cases, the heat transport from the laser-excited hot electrons to the crystal lattice can be described by the two-temperature model [40, 41]. This model treats the electrons and the lattice as two separate systems, where the thermal equilibrium time for the two systems is given by the electron-phonon coupling factor.

However, the process has been found to be rather complex in graphite, where the hot electrons interact with intermediate optical phonons before transferring heat to the lattice through the acoustic phonons [42, 12]. Figure 6.6 illustrates the difference between the two models.

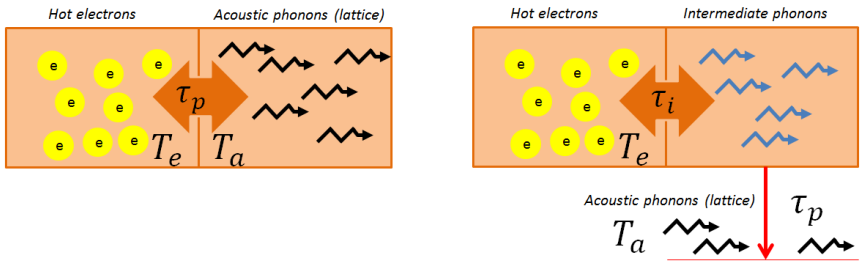

Figure 6.6: Illustration of (a) the two-temperature model and (b) an extended model for graphite including intermediate phonons. T_e and T_a are the electron and lattice temperatures.

To be able to treat these interactions in a simplified way, the process can be modeled by the time-dependent rate equations:

$$\frac{dE_i}{dt} = -\frac{E_i}{\tau_p} + \frac{E_{el}}{\tau_i} \tag{6.4a}$$

$$\frac{dE_a}{dt} = \frac{E_i}{\tau_p} \tag{6.4b}$$

where E_{el}, E_i and E_a are the energy in the electron system, the energy of the intermediate phonons and the energy of the acoustic phonons, respectively, and τ_i and τ_p are the electron-intermediate phonon and intermediate phonon-acoustic phonon time constants. The solution of Equations (6.4a, 6.4b) gives a heat source profile such as that illustrated in Figure 6.7.

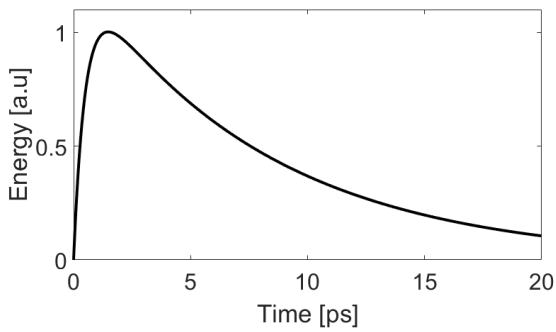

Figure 6.7: Illustration of the kind of heat source profile obtained from the solution of Equation 6.4.

Diffraction curves

The GID_sl online program, which can be accessed on the Stepanov X-ray server [43, 44], is a tool used to simulate X-ray diffraction curves from strained crystals. The simulated strain profiles in a thin film of graphite can be imported into the server using a MATLAB script, and a collection of simulated diffraction curves can be saved for further analysis. Figure 6.8 shows the graphical interface of the symmetric Bragg diffraction template available on the server, where the diffraction geometry and layer profiles can be implemented.

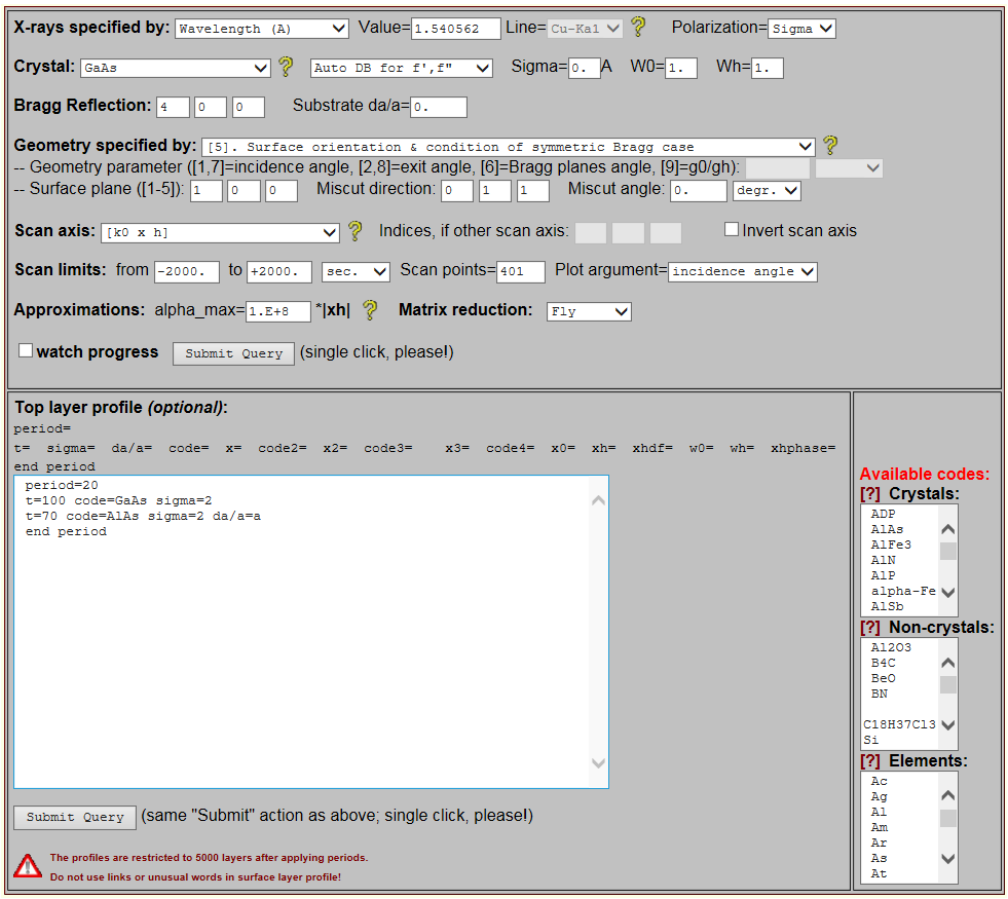

Figure 6.8: The graphical interface of the GID_sl on the Stepanov X-ray server [43, 44].

Chapter 7

X-ray sources

A number of different sources can be used to produce short pulses of X-ray radiation, for example, laser-generated X-ray sources [45], synchrotron radiation facilities based on storage rings, and sources based on linear accelerators (LINAC). One of the experiments presented in this thesis (Paper III) was conducted at a synchrotron beamline at the European Synchrotron Radiation Facility (ESRF) in Grenoble, France. Four other experiments (Paper I, IV, V and VI) were carried out at the FemtoMAX beamline at the MAX IV Laboratory in Lund, Sweden, which is a LINAC-based X-ray radiation source (Paper II).

In a synchrotron, electrons are first accelerated to relativistic energies in a LINAC using high-power electromagnetic radio-frequency (RF) fields produced by a number of RF amplifiers, such as klystrons [46]. These electrons are then stored in a storage ring, where they are collected in bunches. However, the electron bunches become degraded over time in the storage ring due to repulsive Coulomb interactions. In comparison, LINAC-based sources generate X-ray pulses directly from single, accelerated electron bunches in the LINAC, without any storage. LINAC-based sources allow compression and modification of the electron bunches to provide short, intense X-ray pulses [47]. The most intense X-ray pulses are achieved using free electron lasers (FEL), such as the Linac Coherent Light Source (LCLS) at Stanford University, which provides coherent X-ray pulses with pulse durations < 100 fs and 10^{12} photons per pulse [48].

7.1 X-ray insertion devices

Since an accelerating charge emits light the accelerated electrons from a synchrotron storage ring or a LINAC can be used to produce X-ray pulses. To generate light, the electrons can be bent using single magnets, or by periodic series of magnets, usually referred to as wigglers or undulators.

7.1.1 Bending magnets

The simplest device is a single magnet that will bend the electrons and consequently emitting light. A magnet that bends electrons with a bending radius R will emit light with a critical energy, E_c, in eV as [46]:

$$E_c = \frac{3\gamma^3 hc}{4\pi eR} \tag{7.1}$$

where h, c and e are Planck's constant, the speed of light in vacuum, and the elementary charge, respectively, and γ is the relativistic constant $\gamma = 1/\sqrt{1-(v_e/c)^2}$, where v_e is the velocity of the electrons. A bending magnet produces a broad spectrum of light, and E_c is defined such that half the energy is radiated above this value and half below.

7.1.2 Undulators

Undulators are periodic structures of magnets with alternating polarities, as illustrated in Figure 7.1. When an electron passes through an undulator, the light emitted at each magnet will add coherently with the light emitted from a previous one. If the amplitude of the electron path is large enough, the contributions from each magnet will instead add incoherently, and the device is then called a wiggler. The energy E_u generated by an undulator with a magnetic flux density B and period λ_u is given by [46]:

$$E_u = \frac{2n\gamma^2 hc}{\lambda_u e}\left(1 + \frac{K^2}{2} + \theta_e^2\gamma^2\right), \quad K = \frac{eB\lambda_u}{2\pi m_e c} \tag{7.2}$$

where n, θ_e and m_e are the harmonic order, the angle of radiation relative to the optical axis, and the electron rest mass, respectively. The parameter K is called the undulator parameter, and is a measure of the undulator strength.

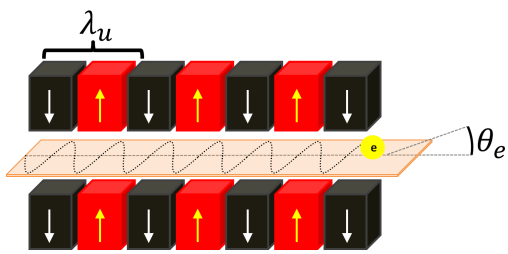

Figure 7.1: Illustration of an electron passing through an undulator with periodically alternating direction of the magnetic fields, indicated by the arrows. The electron trajectory will oscillate in the plane perpendicular to the magnetic fields and generate light with energy given by Equation 7.2.

7.2 The FemtoMAX beamline

During normal operation, the duration of X-ray pulses produced by synchrotron rings is on the order of 100 ps [23], which limits the time resolution possible in experiments. There are methods of shortening the pulse duration in storage rings, such as low-alpha mode [49] and femtoslicing [50], but these have drawbacks in that they lead to a lower flux at the beamline, or the synchrotron facility in general. In addition, the number of FELs available is not sufficient to satisfy the demand for the many experiments that require femtosecond X-ray pulses. The FemtoMAX beamline is a short-pulsed X-ray beamline dedicated to producing ultrashort X-ray pulses, and currently provides pulses with a duration of $\sim$100 fs and 10^7 photons per pulse.

7.2.1 The laser

The laser system at the FemtoMAX beamline consists of a KM Labs Ti:sapphire amplifier that currently delivers 13 mJ pulses centered at a wavelength of 800 nm, with a repetition rate of 100 Hz. An optical parametric amplifier, capable of delivering tunable pulses with central wavelengths of 0.2-10 μm is also available, and is pumped by the amplified 800 nm laser pulses. Synchronization is achieved between the laser and X-ray pulses by locking the RF signal from the LINAC to the laser oscillator. The relative delay between the laser pulse and the X-ray pulse is adjusted by modifying the phase of the RF signal with a phase shifter, giving accurate delays for pump-probe experiments.

7.2.2 Sample environment

The experimental station currently provides an ultrahigh-vacuum sample environment ($< 10^{-8}$ mbar) in a GIXS geometry. The sample position in the GIXS geometry has a temperature-controlled environment that allows sample cooling, using liquid nitrogen or helium, and resistive heating. From the laser hutch, located on the floor above the experimental hutch, the laser beam is transported to the experimental station through a vacuum system including focusing and reflective optics to adjust the beam profile on the sample.

7.2.3 Beamline equipment

Two in-vacuum undulators at the beamline are capable of producing X-rays in the energy range of 1.8 - 20 keV. The beamline is equipped with a series of monochromators for the extraction of monochromatic light. These include double crystal monochromators (DCMs) and multilayer (ML) monochromators. In the present work, an InSb DCM with a bandwidth of $4 \cdot 10^{-4}$ and a Ni-B_4C ML monochromator with a bandwidth of 10^{-2} were used. The X-ray signal is detected by diodes that measure the number of X-ray photons at several positions along the beamline.

Chapter 8

Experiments

This chapter describes the experiments performed on graphite and InSb at the FemtoMAX beamline at the MAX IV laboratory, and at the ID09 beamline at ESRF

8.1 X-ray switch based on a gold-coated InSb crystal

In this study an X-ray switch was developed, and was the first study carried out at the FemtoMAX beamlime during commissioning (Paper I). This switch was based on the generation of coherent acoustic phonons in InSb [21, 22]. In contrast to generating phonons directly by pumping the InSb crystal with a laser, the crystal was instead coated with a gold film that was pumped by the laser, and allowing a train of strain waves to be transmitted into the sample, as illustrated in Figure 8.1 (a).

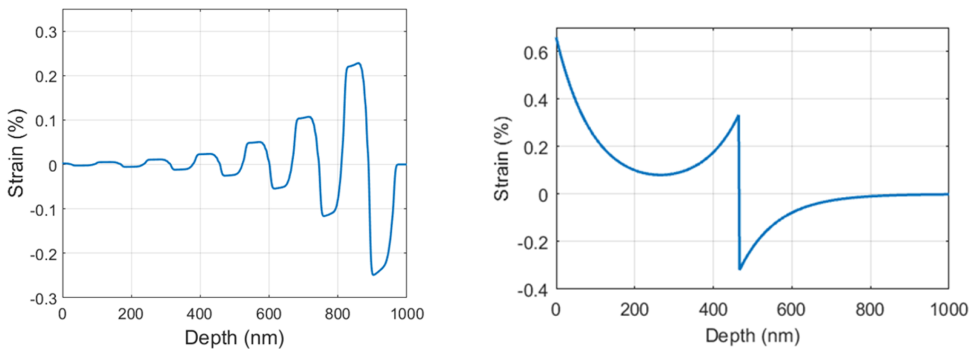

Figure 8.1: Simulated strain profile in InSb, with a gold coating (a) and without a gold coating (b).

This was done in order to modify the spectrum of the phonons in InSb to enhance or cancel phonon modes. The properties of modulation were determined by the material and the thickness of the film. This is in contrast to a single strain pulse generated by direct irradiation of an uncoated sample of InSb by a laser pulse, as illustrated in Figure 8.1 (b). Simulations of the modulation were carried out using the software udkm1Dsim toolbox [51], in which the two-temperature model was used to simulate the heat deposition, strain propagation, and X-ray scattering signals.

A suitable coating material is needed in order to make a fast switch while maintaining high diffraction efficiency. Persson *et al.* [19] investigated an optoacoustic transducer of nickel. However, the peak diffraction efficiency was found to be only 0.2% in their study.

In the present study, gold was found to be a good candidate. The longitudinal speed of sound in gold is slower than in most metals [52], making it possible to design a switch with an acoustic propagation time through the film that is shorter than the electron-phonon coupling time. This is important to generate a uniform high-amplitude strain in the film, while keeping the film thin enough to generate strain waves with a short periodicity. The periodicity of the train of strain waves in InSb, T_{InSb}, corresponds to the enhancement or cancellation of phonon modes. A short periodicity may be desirable in order to cancel out higher-order phonon modes and thus decrease the switch pulse duration. Phonon modes with a periodicity of $n \times T_{InSb}$ will experience enhancement if n is an odd integer, and cancellation if n is an even integer.

The 2D map in Figure 8.2 (a) shows the simulated X-ray diffraction intensity as a function of X-ray energy offset and time delay after laser excitation using an InSb sample with a 60 nm thick gold coating, i.e., the same film thickness as used in the experiment.

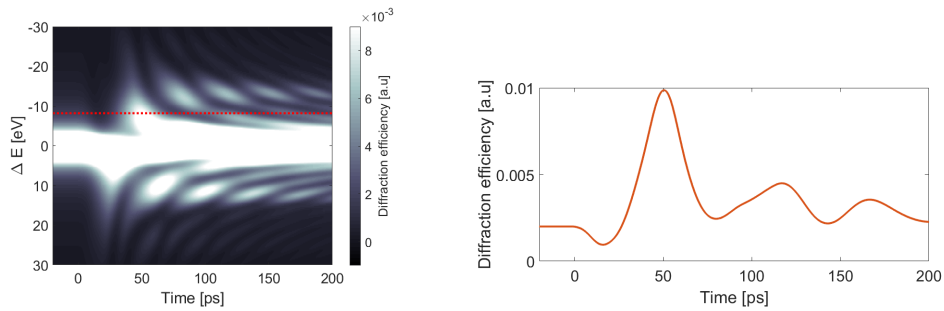

Figure 8.2: (a) A 2D map of simulated diffraction intensity of InSb with gold coating. The red dashed line indicates the first cancelled phonon mode. (b) Lineout at an energy offset of $\Delta E = -8eV$.

This 2D map is the result of the diffraction condition in Equation 4.4 from an InSb (111) Bragg peak centered at an X-ray energy of 5 keV. A lineout at an energy offset of -8 eV is shown in Figure 8.2 (b), and corresponds to the first theoretically cancelled phonon

mode in the experiment. The experimental data acquired at an energy offset of -8 eV were in good agreement with the simulation at an energy offset of -8.2 eV, shown in Figure 8.3. It was found that the diffraction efficiency at a time delay of 50 ps corresponded to a 20 ps X-ray pulse (FWHM) for this switch.

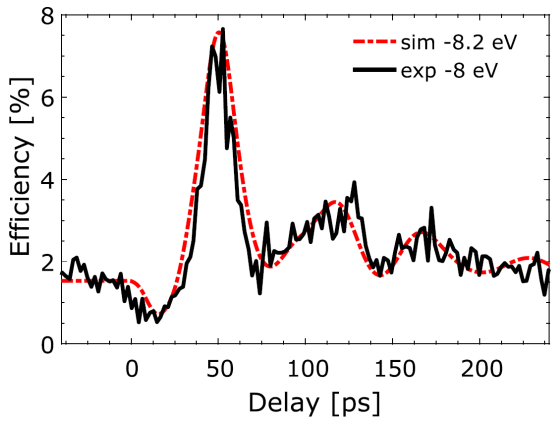

Figure 8.3: The experimental data and simulation of the gold-coated InSb X-ray switch (from Paper I).

8.2 Generation of large compressive strain in graphite

In this study, the laser-induced strain and pressure in a single crystalline natural graphite flake were investigated (Paper III). The experiment was carried out at the ID09 beamline at ESRF. A laser pulse centered at 800 nm wavelength with a pulse duration of 1.2 ps and a fluence exceeding the ablation threshold of graphite were used to induce the strain pulse in the sample. The angle of incidence of the X-rays relative to the sample surface was 12°, and an X-ray energy of 15 keV was used. The sample was azimuthally scanned to ensure that the Bragg condition was fulfilled for the (103) reflection on the 2D detector, which was 78 mm away from the sample. The X-ray pulse duration was 100 ps.

The strain was evaluated at two different times after laser excitation. The effect of strain on the graphite layers was seen as an intensity streak towards higher q values than those seen from the static reflection. Difference images were constructed between the static image before laser excitation and the image acquired at each time delay in order to enhance the contrast of the streak. The experimental difference image at time $t = 100ps$ after laser irradiation is shown in Figure 8.4.

A streak is clearly visible, and the upward direction, towards higher q values, indicates that the strain is due to compression since the interplanar distance d_{103} must be reduced to increase the q value. The dashed lines indicate the change in q value when the c-axis is compressed. The lowest line corresponds to the static q value, and the lines above indicate

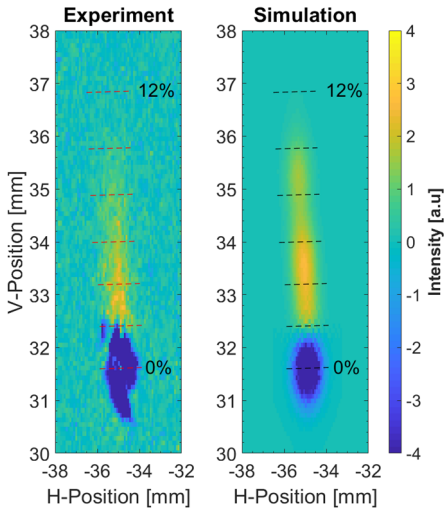

Figure 8.4: Difference image of the experimental diffraction intensity of the (103) reflection at $t = 100ps$ (left) and the corresponding simulation (right).

increasing compression in steps of 2%. A maximum compression of 10% was found along the c-axis, which agrees well with the simulation using the diffraction code [37], where the simulated strain from the hydrodynamic simulation [36] was used as input.

The number of strained layers in the graphite sample could be estimated by comparing the simulation and the experimental data assuming that the intensity of the streak is proportional to the number of strained layers. By comparing the intensity at each time with the unperturbed reflection, the width of layers with a strain exceeding 2% was estimated to be 210 nm and 260 nm at 100 ps and 200 ps, respectively. The broadening of the strain wave and the fact that the initial velocity exceeded the speed of sound along the c-axis [53] indicate the properties of a shock wave.

The amplitude of the pressure wave induced in the sample can be calculated from the bulk modulus of graphite. However, this stress-strain relationship is only valid for small strains. At the values observed in this study the relation between the pressure and interlayer compression is nonlinear. According to studies by Lynch *et al.* [54], 10% compression along the c-axis corresponds to a peak pressure of 7.2 GPa at $t = 100ps$. At $t = 200ps$ the pressure had decreased to 4.8 GPa. As can be seen in Figure 8.5, the pressure induced in the film may provide a means of inducing a direct phase transition to diamond at a low temperature. The hydrodynamic simulation indicated a temperature of only 315 K at the depth of the strain wave after 100 ps, which further supports this hypothesis. This temperature is indicated by the orange dotted line in the figure.

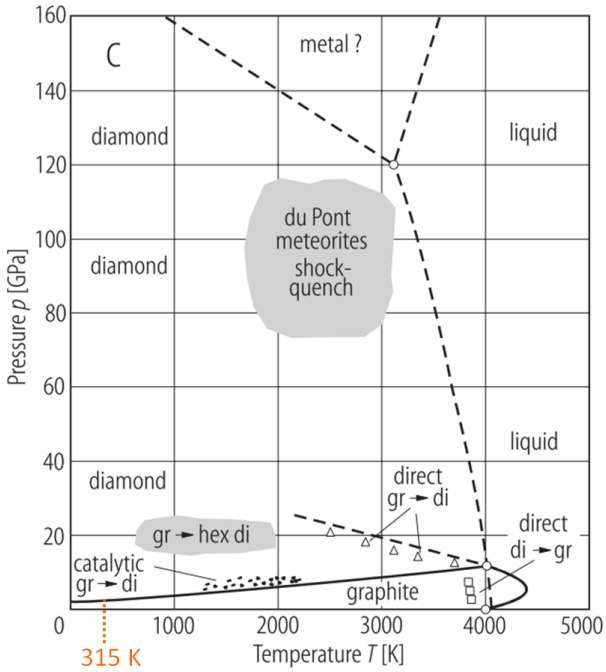

Figure 8.5: Phase diagram of graphite (from [55]). The temperature of 315 K is indicated by the dotted orange line.

8.3 Thermal equilibrium dynamics during non-thermal melting

Non-thermal melting was first considered by Van Vechten *et al.* [27] 40 years ago, when they could not explain the results of experiments performed in their laboratory. Since then, non-thermal melting of InSb has been observed on the sub-picosecond timescale [29]. In 2005 it was suggested that the ultrafast melting process could be explained by the inertial model [15]. This model describes the non-thermal disordering of the atoms forming a liquid state as being dependent on the temperature equilibrium dynamics (see Chapter 5). However, the inertial model was strongly criticized in 2008 [56], and it has not yet been possible to carry out an experiment to test the model. An experiment was therefore carried out to investigate the effect of thermal equilibrium dynamics on non-thermally molten InSb. The thermal equilibrium dynamics were studied during non-thermal melting at sample temperatures ranging from 35 to 500 K (Paper IV).

The sample was an asymmetrically cut InSb wafer with the normal of the (111) plane cut 30° relative to the surface normal. Due to the importance of the X-ray probing depth, the angle of incidence of the X-rays on the sample, θ_{inc}, was calibrated using the external reflection of the X-rays from the sample surface and the direct X-ray beam.

The experiment was set up in a geometry that allowed the spatial coordinates to be

mapped to time, as described in Chapter 5 and Figure 5.4.

An angle of incidence of $45°$ was used for the laser in order to obtain a good spatio-temporal conversion, which was calculated from the geometry to be $14.6 fs/px$, and to ensure a sufficiently high laser fluence along the streak.

Because of the spatio-temporal mapping, the time axis resolution is sensitive to the finite bandwidth of the X-rays diffracted from the sample, and will depend on the sample-detector distance.

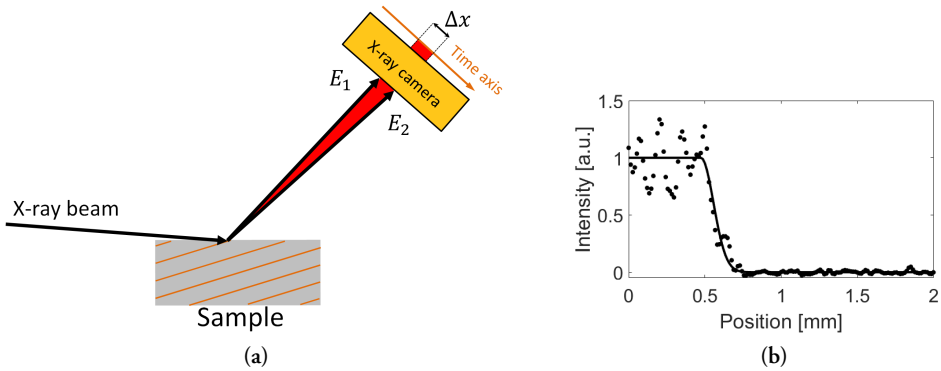

Figure 8.6: (a) Illustration of the spectral smearing. An X-ray beam with a spectral distribution between E_1 and E_2 that diffracts from the sample will lead to an uncertainty Δx. (b) Measured spectral smearing in the experiment (black dots) fitted with a Gaussian function (solid black line).

The influence of the spectral components is illustrated in Figure 8.6 (a) where it is clear that the diffracted X-rays, containing spectral components between E_1 and E_2, from one position on the sample will end up at different positions on the detector. This will lead to smearing of the spatial time axis by an amount Δx. The smearing was measured by placing the edge of a razor blade on the sample and measuring the decrease in diffracted X-ray intensity. Figure 8.6 (b) shows the spectral smearing effect, where Δx was found to be equivalent to a disordering time of 145 fs in with the geometry used in the experiment, which is shorter than the non-thermal melting disordering times measured in this study.

Single shots of the (111) reflection from the InSb sample were captured on the X-ray camera at several sample temperatures. The diffracted intensity along the spatial time axis was evaluated in each shot by fitting the Gaussian Debye-Waller equation (Equation 5.1). Figure 8.7 shows the diffracted intensity from two single shots as a function of time at two different sample temperatures, together with the corresponding fits. It can be seen from the figures that the disordering takes place faster at the higher temperature. The disordering times were extracted from the fits.

The experimental disordering time, τ_{exp}, defined as the time taken for the intensity to fall from 90% to 10% of the initial value, was determined for several sample temperatures

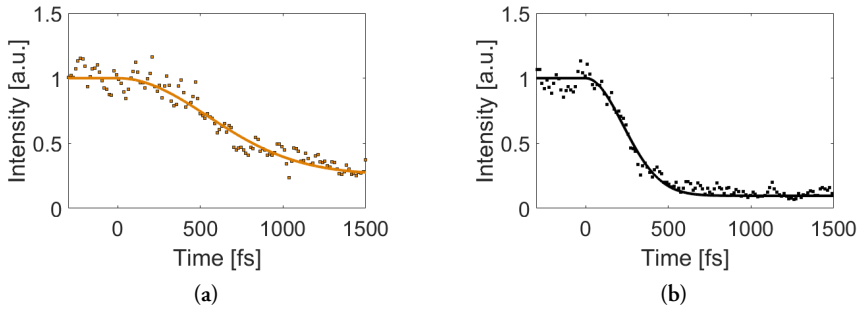

Figure 8.7: Decrease in intensity along the time axis for two single-shot diffraction patterns (orange and black squares), and the corresponding fits (solid lines) for sample temperatures of (a) 70 K and (b) 500 K.

from 35 to 500 K. The values are given in Table 8.1, together with the theoretical values obtained from the inertial model.

The experimental disordering times are in excellent agreement with those predicted by the inertial model at sample temperatures ≥ 70 K, but there was a deviation at low temperatures. First, an accelerating potential was included. However, one important factor for low temperatures was not initially considered in the model. At low temperatures quantum fluctuations must be included in the vibrational energy. For a vibrating crystal lattice this energy is given by the zero-point vibrational energy. Including this gives the following expression for the energy [57]:

$$U_v = \frac{9}{8} k_B T_D + 3 k_B T D_3(T_D/T) \tag{8.1}$$

where k_B, T, T_D and D_3 are the Boltzmann constant, temperature, the Debye temperature and the Debye function, respectively. The first term in Equation 8.1 is the lattice zero-point vibrational energy, and will contribute more to the total energy as the temperature decreases. At higher temperatures, above the Debye temperature, the second term

Table 8.1: Theoretical and measured disordering times during non-thermal melting at different sample temperatures.

Temperature [K]	Classical theory [fs]	Quantum theory [fs]	Experiment [fs]
500	380	380	410 ± 40
300	490	490	470 ± 50
150	690	670	760 ± 60
70	1010	910	960 ± 110
35	1430	1050	1000 ± 80

will dominate, and will approach the classic result of $U_{cl} = 3k_BT$. The inertial model described by the energy in Equation 8.1 was found to be in excellent agreement with the experimental data without the need for an accelerating potential, as can be seen in Figure 8.8.

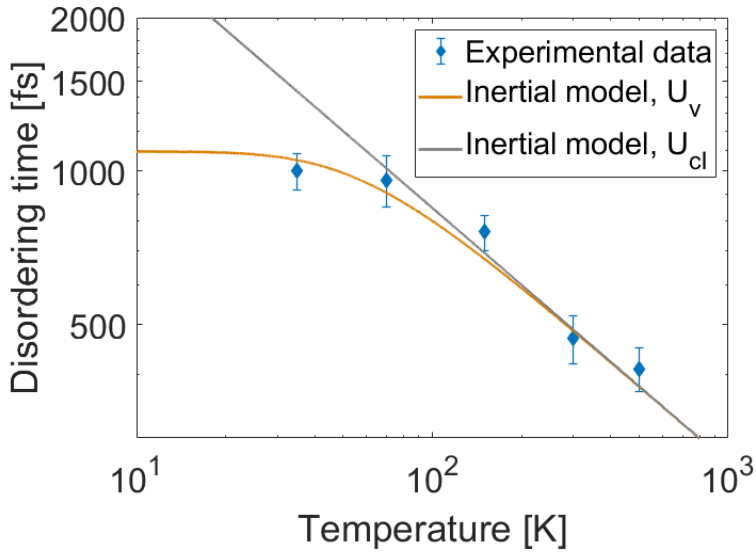

Figure 8.8: The disordering time as a function of sample temperature. The experimental data (blue diamonds) are shown together with the results of the calculations using the inertial model with classical vibrational energy (gray curve). The orange curve shows the disordering times predicted by the inertial model including the zero-point energy (Equation 8.1).

The results of the calculations show that the disordering of the atoms is more accurately predicted by the inertial model, than the model proposed by Zijlstra *et al.* [56], which predicts that the disordering time is independent of the sample temperature.

The property of the constant disordering time at thermal equilibrium during non-thermal melting was studied further (Paper V) to investigate the optimal conditions of a timing monitor based on repetitive non-thermal melting of InSb. This is further discussed in Section 8.5.

8.4 Thermal conductivity of a thin graphite film

Experiments were carried out to study the cross-plane thermal conductivity of a thin graphite film (Papar VI). The study was performed by depositing heat with a laser pulse and using X-ray diffraction to probe the strain relaxation, and was carried out at the FemtoMAX

beamline at the MAX IV laboratory. The sample was a thin film of graphite grown by chemical vapor deposition on a nickel substrate [58].

Timed scans were used up to probe the strain relaxation, where the delay between the laser and the X-ray pulses was changed on the picosecond timescale. The diffracted (002) reflection from the graphite film was recorded at each delay with a detector at a distance 125 mm away from the sample. The series of images of the X-ray reflection was then analyzed by calculating the average displacement of the Bragg reflection as a function of time.

The thickness of the graphite film must be known as the cross-plane thermal conductivity is expected to vary with the thickness in thin films [59, 60]. The thickness of the film was determined at the same position on the sample as the conductivity measurements. The transient acoustic response of the graphite film could be used to measure its thickness due to the picosecond temporal resolution. The periodic variation in the transient response resulting from interference between the propagating and reflected strain waves in the film, was reproduced with the same periodicity as predicted by the simulations, as can be seen in Figure 8.9 (a). As an illustration an arbitrarily simulated thickness of 60 nm is illustrated in Figure 8.9 (b).

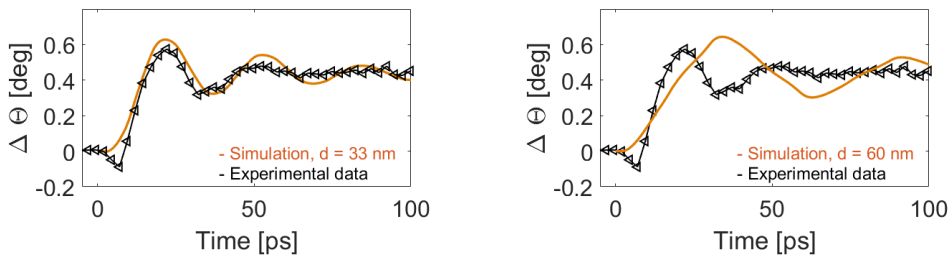

Figure 8.9: Periodic variation in the Bragg angle in the graphite film as a function of time delay between the laser and X-ray pulses of up to 100 ps. The best agreement with the simulations indicated a film thickness of 33 nm. (b) A simulated film thickness of 60 nm.

Several simulations with different thicknesses were carried out and the best agreement was found to be 33 nm from the sum of the squared residuals between the experimental data and the simulations. A compressive induced strain can be seen in the experimental data in Figure 8.9 during the first 10 ps. This was attributed to the property of graphite being a saturable absorber, which means that the absorption depth changes upon laser irradiation [8]. An increase in the absorption depth in the graphite film will lead to an increase in the heating of the underlying substrate, thus compressing the graphite layers at the film-substrate interface as the substrate expands thermally. A transient compressive strain was seen in the simulations as the absorption depth was increased. However, the absorption properties were not further investigated in this study as the thermal conductivity was measured from the strain relaxation.

Using the thickness of the graphite film, the strain relaxation was found to fit a simulation with a thermal conductivity of κ = 0.5 W/m-K, as shown in Figure 8.10. This result is close to previously measured values for graphite films of similar thickness at room temperature [38, 61]. However, in contrast to previous measurements, the film thickness was measured at the same position on the sample as the thermal conductivity measurements in the current study.

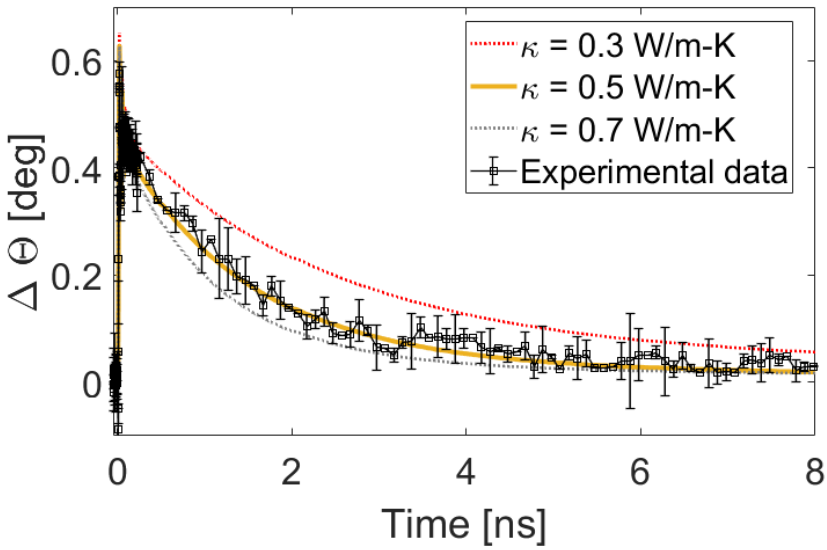

Figure 8.10: Experimental data and simulations showing the deviation in Bragg angle as a function of time delay for the first 8 ps, for a film thickness of 33 nm. The best fit was found for a thermal conductivity of 0.5 W/m-K, indicated by the solid orange curve. The dotted curves show simulations at thermal conductivities of 0.3 W/m-K and 0.7 W/m-K.

8.5 Non-thermal melting as a timing monitor

X-ray timing diagnostics of the deviation (jitter) and the difference in arrival time between the laser and the X-ray pulses in a pump-probe experiment is important to be able to carry out experiments on femtosecond dynamics. Due to the ultrafast timescale of non-thermal melting, repetitive non-thermal melting has been suggested as a timing tool [62], and the properties of non-thermal melting have also been used to verify other timing tools [63]. The optimal conditions for repetitive non-thermal melting and regrowth of InSb were investigated in an experiment at the FemtoMAX beamline (Paper V).

The experimental geometry was as described in Section 8.3. A number of single shots were made at the same sample position. The decrease in intensity along the temporally

mapped diffraction streak and the degradation of the diffraction intensity were analyzed after each shot. The time at which the intensity had fallen to 50% of its initial value was used as the reference time, referred to as $t = 0$. Experiments were repeated at sample temperatures between 300 and 500 K.

The diffraction intensity after multiple shots was found to decrease less at a sample temperature of 500 K than at lower temperatures. Hence, the reference time could be determined after more than 100 shots, compared to measurements at room temperature, where the sample degraded rapidly, after only a few shots, as can be seen in Figure 8.11.

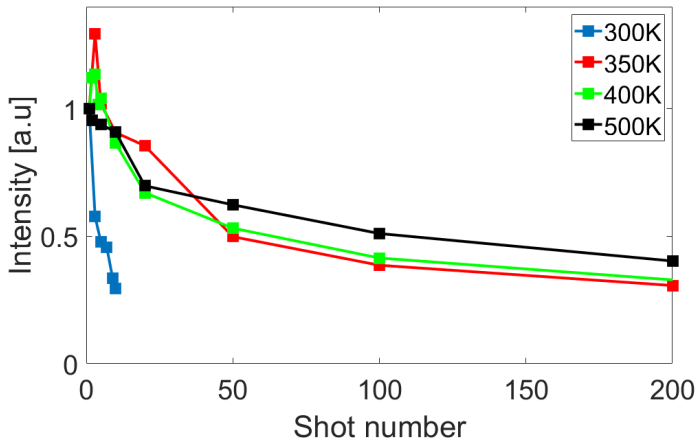

Figure 8.11: X-ray diffraction intensity as a function of number of shots at different sample temperatures. Rapid degradation of the sample was seen after only a few shots at room temperature.

However, the visual contrast in determining the decrease in diffraction intensity resulting from non-thermal melting at higher sample temperatures was found to be limited by laser-induced periodic surface structures [64, 65]. The position on the spatio-temporal streak at which the diffraction intensity had fallen to 50% of the initial intensity was extracted for each shot to investigate the performance of a jitter monitor based on an RF cavity at the FemtoMAX beamline. The precision of the jitter monitor was determined to be 600 fs in this study.

It can be noted that there is a slower degrading during the regrowth at higher temperatures. Further time-resolved studies were carried out to investigate the velocity of regrowth. The regrowth velocity of InSb has previously been suggested to be a limiting factor in ordered re-crystallization after laser excitation [66]. Figure 8.12 shows the diffracted X-ray intensity as a function of time after laser irradiation.

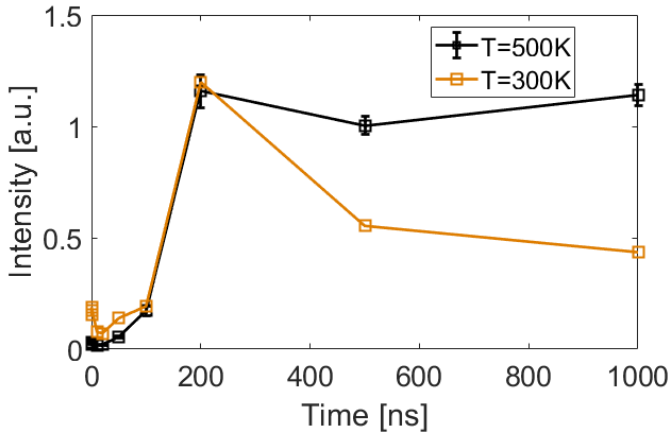

Figure 8.12: Time-resolved X-ray intensity during regrowth of InSb at sample temperatures of 300 K and 500 K.

A notable difference in intensity can be seen at times $\geq$ 500 ns at sample temperatures of 300 K and 500 K. No significant difference was seen in the regrowth rate at shorter times, and further investigations are required before any conclusions can be drawn concerning the regrowth velocity. One possible explanation of the difference in intensity could be that the lower thermal conductivity of InSb at 500 K leads to a reduction in the regrowth velocity, and hence the sample re-crystallizes with fewer impurities than at room temperature.

Chapter 9

Summary & Outlook

9.1 Summary

The experiments described in this thesis were focused on two materials, graphite and InSb. Both materials were studied above and below the damage threshold from short-pulse laser irradiation with a central wavelength of 800 nm, and probed using X-ray diffraction. In graphite, a strain of 10% was observed close to room temperature, which generated a pressure of 7.2 GPa. It was therefore concluded that it is possible to directly induce a graphite-diamond transformation through pressure in a natural graphite sample using an intense laser pulse. The unique heat conduction properties along the c-axis was determined for a thin graphite film grown on a nickel substrate. A cross-plane thermal conductivity of 0.5 W/m-K was found for a graphite film with a thickness of 33 nm. The thickness and thermal conductivity of the film were determined at the same time and at the same position on the sample.

Phonons and non-thermal melting were studied in InSb. It was shown that short X-ray pulses of 20 ps could be obtained by the generation and modification of coherent acoustic phonons in InSb. To modify the phonon spectrum, the InSb sample was coated with a 60 nm gold film, which enhanced or cancelled out specific phonon modes in the sample due to the acoustic echoes transmitted by the gold film. In the case of non-thermal melting, the inertial model of atomic disordering was investigated. By cooling and heating the InSb sample and studying the disordering time, it was concluded that the disordering time followed the inertial model. It was also concluded that the zero-point vibrational energy had to be included in the model in order to describe the dynamics at lower temperatures. Repetitive non-thermal melting and regrowth of InSb was also investigated, and it was found that the degeneration of the sample was lower at higher sample temperatures. It was also demonstrated that this could be used as a timing tool at synchrotron radiation facilities.

9.2 Outlook

Most of the experiments presented in this thesis were carried out at the FemtoMAX beamline, demonstrating the importance of an alternative short-pulsed X-ray source to FELs. The experiments were part of the important commissioning activities towards making the beamline available for user experiments.

9.2.1 2D materials

Time-resolved X-ray diffraction experiments may be challenging in 2D materials, due to the weak X-ray scattering. As the FemtoMAX beamline is developed towards higher repetition rates, it will be possible to carry out studies of 2D materials using time-resolved X-ray diffraction in a reasonable time. 2D materials have attracted considerable interest due to their exotic properties [67], and ultrafast X-ray diffraction studies could reveal as yet unknown dynamics on the fs-ps timescale.

9.2.2 THz-pump-X-ray-probe experiments

X-ray diffraction experiments using a laser-induced THz pump source were also carried out at the FemtoMAX beamline, although this was not part of the work included in this thesis. The development of a THz pump source producing intense THz pulses is part of the ongoing work at the beamline to allow time-resolved THz-pump-X-ray-probe experiments to be carried out. THz pump experiments have recently become the subject of considerable interest due to the possibility of direct excitation of lower energy states and the high-peak electric fields that can be generated [68]. Due to the femtosecond time duration of the X-ray pulses, this setup can be used to study, for example, sample responses on a sub-cycle time scale [69].

9.2.3 Regrowth of InSb

The temperature-dependent regrowth of InSb was clearly shown to have a significant impact on the performance of a timing monitor based on repetitive non-thermal melting (Paper V). However, too little data were obtained to allow any convincing conclusions to be drawn about the physics of regrowth, such as the properties that may govern the regrowth velocity, of whether the regrowth velocity is modified by thermal conductivity. Single shots could also be performed at different time delays to improve the quality of the data. The data in Figure 8.12 were measured at the same sample position for each sample temperature, and degradation effects may therefore have contributed significantly to the data acquired.

The Author's Contributions

Paper I

"Communication: Demonstration of a 20 ps X-ray switch based on a photoacoustic transducer"
A. Jarnac, Xiaocui Wang, Å. U. J. Bengtsson, J. C. Ekström, H. Enquist, A. Jurgilaitis, D. Kroon, A. I. H. Persson, V.-T. Pham, C. M. Tu, and J. Larsson. Structural Dynamics 4, 051102 (2017)

This paper describes an X-ray switch designed to reduce the duration of an X-ray pulse from 100 ps to 20 ps. I participated during the experimental beamtime and performed some data analysis on-site. I also participated in sample preparation at the Lund Nano Lab where the sample was coated. I also gave feedback on the manuscript.

Paper II

"FemtoMAX - an X-ray beamline for structural dynamics at the short-pulse facility of MAX IV"
H. Enquist, A. Jurgilaitis, A. Jarnac, Å. U. J. Bengtsson, M. Burza, F. Curbis, C. Disch, J. C. Ekström, M. Harb, L. Isaksson, M. Kotur, D. Kroon, F. Lindau, E. Mansten, J. Nygaard, A. I. H. Persson, V. T. Pham, M. Rissi, S. Thorin, C.-M. Tu, E. Wallén, X. Wang, S. Werin and J. Larsson. J. Synchrotron Rad. 25, 570-579 (2018)

This paper describes the FemtoMAX beamline at the MAX IV laboratory. I participated in experiments during commissioning of the beamline and gave feedback on the manuscript.

Paper III

"Generation of a large compressive strain wave in graphite by ultrashort-pulse laser irradiation"
Xiaocui Wang, A. Jarnac, J. C. Ekström, Å. U. J. Bengtsson, F. Dorchies, H. Enquist, A. Jurgilaitis, M. N. Pedersen, C.-M. Tu, M. Wulff, and J. Larsson. Structural Dynamics 6, 024501 (2019)

This paper describes the generation of a large compressive strain wave in a natural graphite sample during laser irradiation. I participated in setting up the sample at the ID09 beamline at ESRF, and in data analysis, both on-site and after the experiment, as well as in some of the sample characterization measurements. I also gave feedback on the manuscript.

Paper IV

"Role of thermal equilibrium dynamics in atomic motion during nonthermal laser-induced melting"
Xiaocui Wang, J. C. Ekström, Å. U. J. Bengtsson, A. Jarnac, A. Jurgilaitis, Van-Thai Pham, D. Kroon, H. Enquist, and J. Larsson. Phys. Rev. Letters 124, 105701 (2020)

This paper describes the thermal equilibrium dynamics during non-thermal melting of InSb. I participated in the planning of the experiment, sample preparation, and data acquisition. I also took part in the data analysis, and wrote some of the analysis scripts used. I also gave feedback on the manuscript. I produced some of the figures and wrote parts of the first draft of the supplementary information.

Paper V

"Repetitive non-thermal melting as a timing monitor for femtosecond pump/probe X-ray experiments"
Å. U. J. Bengtsson, J. C. Ekström, Xiaocui Wang, A. Jurgilaitis, Van-Thai Pham, D. Kroon and J. Larsson. Submitted (2020)

This paper describes the optimization of a time monitor tool based on non-thermal melting of InSb. I participated in the acquisition and analysis of the data during the experiment, and also wrote some of the analysis scripts. I also gave feedback on the manuscript.

Paper VI

"Acoustic response and cross-plane thermal conductivity of a thin graphite film measured with time-resolved X-ray diffraction"
J. C. Ekström, Å. U. J. Bengtsson, S. Checchia, H. Coudert-Alteirac, A. Jurgilaitis, D. Kroon, A. N. Obraztsov, V.-T. Pham, C. C. Popescu, A. Stenquist, and J. Larsson. Submitted (2020)

This paper describes an accurate method of determining the thermal conductivity in a thin film of graphite, together with the results obtained. I led the planning of the experiment, and performed the data analysis on-site and after the experiment. I also performed the simulations presented in the paper. In addition, I wrote the first draft of the manuscript and produced the figures.

References

[1] William Henry Bragg and William Lawrence Bragg. The reflection of x-rays by crystals. *Proceedings of the Royal Society of London. Series A, Containing Papers of a Mathematical and Physical Character*, 88(605):428–438, 1913.

[2] Donna Strickland and Gerard Mourou. Compression of amplified chirped optical pulses. *Optics Communications*, 56(3):219–221, 1985.

[3] Bahaa E. A Saleh and Malvin Carl Teich. *Fundamentals of photonics*. John Wiley & sons, Inc., Hoboken, New Jersey, 2007.

[4] Matthias C Hoffmann and József András Fülöp. Intense ultrashort terahertz pulses: generation and applications. *Journal of Physics D: Applied Physics*, 44(8):083001, feb 2011.

[5] Mostafa Shalaby, Carlo Vicario, Karunanithi Thirupugalmani, Srinivasan Brahadeeswaran, and Christoph P. Hauri. Intense thz source based on bna organic crystal pumped at ti:sapphire wavelength. *Opt. Lett.*, 41(8):1777–1780, Apr 2016.

[6] Christoph P. Hauri, Clemens Ruchert, Carlo Vicario, and Fernando Ardana. Strong-field single-cycle thz pulses generated in an organic crystal. *Applied Physics Letters*, 99(16):161116, 2011.

[7] S S Dhillon, M S Vitiello, E H Linfield, A G Davies, Matthias C Hoffmann, John Booske, Claudio Paoloni, M Gensch, P Weightman, G P Williams, E Castro-Camus, D R S Cumming, F Simoens, I Escorcia-Carranza, J Grant, Stepan Lucyszyn, Makoto Kuwata-Gonokami, Kuniaki Konishi, Martin Koch, Charles A Schmuttenmaer, Tyler L Cocker, Rupert Huber, A G Markelz, Z D Taylor, Vincent P Wallace, J Axel Zeitler, Juraj Sibik, Timothy M Korter, B Ellison, S Rea, P Goldsmith, Ken B Cooper, Roger Appleby, D Pardo, P G Huggard, V Krozer, Haymen Shams, Martyn Fice, Cyril Renaud, Alwyn Seeds, Andreas Stöhr, Mira Naftaly, Nick Ridler, Roland Clarke, John E Cunningham, and Michael B Johnston. The 2017 terahertz science and technology roadmap. *Journal of Physics D: Applied Physics*, 50(4):043001, jan 2017.

[8] F. Carbone, G. Aubock, A. Cannizzo, F. Van Mourik, R.R. Nair, A.K. Geim, K.S. Novoselov, and M. Chergui. Femtosecond carrier dynamics in bulk graphite and graphene paper. *Chemical Physics Letters*, 504(1):37 – 40, 2011.

[9] Markus Breusing, Claus Ropers, and Thomas Elsaesser. Ultrafast carrier dynamics in graphite. *Phys. Rev. Lett.*, 102:086809, Feb 2009.

[10] Eric Nilsson. Ultrafast transient coherent raman microscopy(tram), 2019. Student Paper.

[11] G. Thomson and A. Reid. Diffraction of cathode rays by a thin film. *Nature*, 119:890, 1927.

[12] M. Harb, H. Enquist, A. Jurgilaitis, F. T. Tuyakova, A. N. Obraztsov, and J. Larsson. Phonon-phonon interactions in photoexcited graphite studied by ultrafast electron diffraction. *Phys. Rev. B*, 93:104104, Mar 2016.

[13] B. E. Warren. *X-ray diffraction*. Dover Publications, Inc., New York, 1990.

[14] E.M. Henke, B.L. Gullikson and J.C. Davis. X-ray interactions: photoabsorption, scattering, transmission, and reflection at e=50-30000 ev, z=1-92. *Atomic Data and Nuclear Data Tables*, 54(2):181–342, 1993.

[15] A. M. Lindenberg, J. Larsson, K. Sokolowski-Tinten, K. J. Gaffney, C. Blome, O. Synnergren, J. Sheppard, C. Caleman, A. G. MacPhee, D. Weinstein, D. P. Lowney, T. K. Allison, T. Matthews, R. W. Falcone, A. L. Cavalieri, D. M. Fritz, S. H. Lee, P. H. Bucksbaum, D. A. Reis, J. Rudati, P. H. Fuoss, C. C. Kao, D. P. Siddons, R. Pahl, J. Als-Nielsen, S. Duesterer, R. Ischebeck, H. Schlarb, H. Schulte-Schrepping, Th. Tschentscher, J. Schneider, D. von der Linde, O. Hignette, F. Sette, H. N. Chapman, R. W. Lee, T. N. Hansen, S. Techert, J. S. Wark, M. Bergh, G. Huldt, D. van der Spoel, N. Timneanu, J. Hajdu, R. A. Akre, E. Bong, P. Krejcik, J. Arthur, S. Brennan, K. Luening, and J. B. Hastings. Atomic-scale visualization of inertial dynamics. *Science*, 308(5720):392–395, 2005.

[16] P. B. Hillyard, K. J. Gaffney, A. M. Lindenberg, S. Engemann, R. A. Akre, J. Arthur, C. Blome, P. H. Bucksbaum, A. L. Cavalieri, A. Deb, R. W. Falcone, D. M. Fritz, P. H. Fuoss, J. Hajdu, P. Krejcik, J. Larsson, S. H. Lee, D. A. Meyer, A. J. Nelson, R. Pahl, D. A. Reis, J. Rudati, D. P. Siddons, K. Sokolowski-Tinten, D. von der Linde, and J. B. Hastings. Carrier-density-dependent lattice stability in insb. *Phys. Rev. Lett.*, 98:125501, Mar 2007.

[17] Henning Bubert and Holger Jenett. *Surface and thin film analysis: principles, instrumentation, applications*. Wiley-VCH, Weinheim, 2002.

[18] C. Thomsen, H. T. Grahn, H. J. Maris, and J. Tauc. Surface generation and detection of phonons by picosecond light pulses. *Phys. Rev. B*, 34:4129–4138, Sep 1986.

[19] A. I. H. Persson, H. Enquist, A. Jurgilaitis, B. P. Andreasson, and J. Larsson. Real-time observation of coherent acoustic phonons generated by an acoustically mismatched optoacoustic transducer using x-ray diffraction. *Journal of Applied Physics*, 118(18):185308, 2015.

[20] Karl W. Böer and Udo W. Pohl. *Elasticity and Phonons*, pages 1–40. Springer International Publishing, Cham, 2020.

[21] A. M. Lindenberg, I. Kang, S. L. Johnson, T. Missalla, P. A. Heimann, Z. Chang, J. Larsson, P. H. Bucksbaum, H. C. Kapteyn, H. A. Padmore, R. W. Lee, J. S. Wark, and R. W. Falcone. Time-resolved x-ray diffraction from coherent phonons during a laser-induced phase transition. *Phys. Rev. Lett.*, 84:111–114, Jan 2000.

[22] J. Larsson, A. Allen, P. Bucksbaum, et al. Picosecond x-ray diffraction studies of laser-excited acoustic phonons in insb. *Appl. Phys. A*, 75:467–478, Oct 2002.

[23] P.H. Bucksbaum and R. Merlin. The phonon bragg switch: a proposal to generate sub-picosecond x-ray pulses. *Solid State Communications*, 111(10):535 – 539, 1999.

[24] Peter Gaal, Daniel Schick, Marc Herzog, André Bojahr, Roman Shayduk, Jevgeni Goldshteyn, Wolfram Leitenberger, Ionela Vrejoiu, Dmitry Khakhulin, Michael Wulff, and Matias Bargheer. Ultrafast switching of hard X-rays. *Journal of Synchrotron Radiation*, 21(2):380–385, Mar 2014.

[25] O. Synnergren, T. N. Hansen, S. Canton, H. Enquist, P. Sondhauss, A. Srivastava, and J. Larsson. Coherent phonon control. *Applied Physics Letters*, 90(17):171929, 2007.

[26] B. Rethfeld, K. Sokolowski-Tinten, D. von der Linde, et al. Timescales in the response of materials to femtosecond laser excitation. *Appl. Phys. A*, 79:767–769, 2004.

[27] J. A. Van Vechten, R. Tsu, F. W. Saris, and D. Hoonhout. Reasons to believe pulsed laser annealing of si does not involve simple thermal melting. *Physics Letters A*, 74(6):417 – 421, 1979.

[28] C. V. Shank, R. Yen, and C. Hirlimann. Time-resolved reflectivity measurements of femtosecond-optical-pulse-induced phase transitions in silicon. *Phys. Rev. Lett.*, 50:454–457, Feb 1983.

[29] A. Rousse, C. Rischel, S. Fourmaux, et al. Non-thermal melting in semiconductors measured at femtosecond resolution. *Nature*, 410:65–68, 2001.

[30] O. Synnergren, M. Harbst, T. Missalla, J. Larsson, G. Katona, R. Neutze, and R. Wouts. Projecting picosecond lattice dynamics through x-ray topography. *Applied Physics Letters*, 80(20):3727–3729, 2002.

[31] Jiayan Luo, Xin Zhao, Jinsong Wu, Hee Dong Jang, Harold H. Kung, and Jiaxing Huang. Crumpled graphene-encapsulated si nanoparticles for lithium ion battery anodes. *The Journal of Physical Chemistry Letters*, 3(13):1824–1829, 2012. PMID: 26291867.

[32] K. S. Novoselov, A. K. Geim, S. V. Morozov, D. Jiang, Y. Zhang, S. V. Dubonos, I. V. Grigorieva, and A. A. Firsov. Electric field effect in atomically thin carbon films. *Science*, 306(5696):666–669, 2004.

[33] A. Balandin. Thermal properties of graphene and nanostructured carbon materials. *Nature Mater*, 10:569–581, 2011.

[34] G. Yang and J. Wang. Pulsed-laser-induced transformation path of graphite to diamond via an intermediate rhombohedral graphite. *Appl. Phys. A*, 72:475–479, 2001.

[35] R. Nüske, A. Jurgilaitis, H. Enquist, M. Harb, Y. Fang, U. Håkanson, and J. Larsson. Transforming graphite to nanoscale diamonds by a femtosecond laser pulse. *Applied Physics Letters*, 100(4):043102, 2012.

[36] J. P. Colombier, P. Combis, F. Bonneau, R. Le Harzic, and E. Audouard. Hydrodynamic simulations of metal ablation by femtosecond laser irradiation. *Phys. Rev. B*, 71:165406, Apr 2005.

[37] M. Harb. Diffraction code URL: https://github.com/maherharb/Diffraction Accessed: 2017-06-23.

[38] M. Harb, C. von Korff Schmising, H. Enquist, A. Jurgilaitis, I. Maximov, P. V. Shvets, A. N. Obraztsov, D. Khakhulin, M. Wulff, and J. Larsson. The c-axis thermal conductivity of graphite film of nanometer thickness measured by time resolved x-ray diffraction. *Applied Physics Letters*, 101(23):233108, 2012.

[39] Alexander Balandin and Kang L. Wang. Effect of phonon confinement on the thermoelectric figure of merit of quantum wells. *Journal of Applied Physics*, 84(11):6149–6153, 1998.

[40] S.I. Anisimov, B.L. Kapeliovich, and T.L. Perel'man. Electron emission from the metal surfaces induced by ultrashort lasers pulses. *Sov. Phys.-JETP*, 39(2), 1974.

[41] A. I. H. Persson, A. Jarnac, Xiaocui Wang, H. Enquist, A. Jurgilaitis, and J. Larsson. Studies of electron diffusion in photo-excited ni using time-resolved x-ray diffraction. *Applied Physics Letters*, 109(20):203115, 2016.

[42] Tobias Kampfrath, Luca Perfetti, Florian Schapper, Christian Frischkorn, and Martin Wolf. Strongly coupled optical phonons in the ultrafast dynamics of the electronic energy and current relaxation in graphite. *Phys. Rev. Lett.*, 95:187403, Oct 2005.

[43] X-Ray Server URL: https://x-server.gmca.aps.anl.gov.

[44] Sergey A. Stepanov. X-ray server: an online resource for simulations of x-ray diffraction and scattering. In Manuel Sanchez del Rio, editor, *Advances in Computational Methods for X-Ray and Neutron Optics*, volume 5536, pages 16 – 26. International Society for Optics and Photonics, SPIE, 2004.

[45] A. Rousse, P. Audebert, J. P. Geindre, F. Falliès, J. C. Gauthier, A. Mysyrowicz, G. Grillon, and A. Antonetti. Efficient kα x-ray source from femtosecond laser-produced plasmas. *Phys. Rev. E*, 50:2200–2207, Sep 1994.

[46] S. Werin. *Accelerator technique, 2.5th ed.* MAX-lab, Lund, 2006.

[47] Sara Thorin, Joel Andersson, Francesca Curbis, Mikael Eriksson, Olivia Karlberg, Dionis Kumbaro, Erik Mansten, David Olsson, and Sverker Werin. The MAX IV Linac. In *Proceedings, 27th Linear Accelerator Conference, LINAC2014: Geneva, Switzerland, August 31-September 5, 2014*, pages 400–403, 2014.

[48] P. Emma, R. Akre, J. Arthur, et al. First lasing and operation of an ångstrom-wavelength free-electron laser. *Nature Photon*, 4:641–647, 2010.

[49] I. P. S. Martin, G. Rehm, C. Thomas, and R. Bartolini. Experience with low-alpha lattices at the diamond light source. *Phys. Rev. ST Accel. Beams*, 14:040705, Apr 2011.

[50] A. A. Zholents and M. S. Zolotorev. Femtosecond x-ray pulses of synchrotron radiation. *Phys. Rev. Lett.*, 76:912–915, Feb 1996.

[51] D. Schick, A. Bojahr, M. Herzog, R. Shayduk, C. von Korff Schmising, and M. Bargheer. udkm1dsim—a simulation toolkit for 1d ultrafast dynamics in condensed matter. *Computer Physics Communications*, 185(2):651 – 660, 2014.

[52] W. Schaaffs. Molecular acoustics · 5.1.2 metals: Datasheet from landolt-börnstein - group ii molecules and radicals · volume 5: "molecular acoustics" in springermaterials (https://doi.org/10.1007/10201218_69). Copyright 1967 Springer-Verlag Berlin Heidelberg.

[53] Alexey Bosak, Michael Krisch, Marcel Mohr, Janina Maultzsch, and Christian Thomsen. Elasticity of single-crystalline graphite: Inelastic x-ray scattering study. *Phys. Rev. B*, 75:153408, Apr 2007.

[54] R. W. Lynch and H. G. Drickamer. Effect of high pressure on the lattice parameters of diamond, graphite, and hexagonal boron nitride. *The Journal of Chemical Physics*, 44(1):181–184, 1966.

[55] Diamond (c) phase diagram, equation of state: Datasheet from landolt-börnstein - group iii condensed matter · volume 41a1α: "group iv elements, iv-iv and iii-v compounds. part a - lattice properties" in springermaterials (https://doi.org/10.1007/10551045_168). Copyright 2001 Springer-Verlag Berlin Heidelberg, Part of SpringerMaterials. Accessed 2020-04-09.

[56] Eeuwe S. Zijlstra, Jessica Walkenhorst, and Martin E. Garcia. Anharmonic noninertial lattice dynamics during ultrafast nonthermal melting of insb. *Phys. Rev. Lett.*, 101:135701, Sep 2008.

[57] K. Nakamura and T. Mohri. Non-empirical calculation of thermal vibration effects on the phase stability of InP-InSb alloy. *Modelling and Simulation in Materials Science and Engineering*, 1(2):143–150, jan 1993.

[58] A.N. Obraztsov, E.A. Obraztsova, A.V. Tyurnina, and A.A. Zolotukhin. Chemical vapor deposition of thin graphite films of nanometer thickness. *Carbon*, 45(10):2017 – 2021, 2007.

[59] Ke Sun, Michael A. Stroscio, and Mitra Dutta. Graphite c-axis thermal conductivity. *Superlattices and Microstructures*, 45(2):60 – 64, 2009.

[60] Zhiyong Wei, Zhonghua Ni, Kedong Bi, Minhua Chen, and Yunfei Chen. Interfacial thermal resistance in multilayer graphene structures. *Physics Letters A*, 375(8):1195 – 1199, 2011.

[61] Qiang Fu, Juekuan Yang, Yunfei Chen, Deyu Li, and Dongyan Xu. Experimental evidence of very long intrinsic phonon mean free path along the c-axis of graphite. *Applied Physics Letters*, 106(3):031905, 2015.

[62] H. Navirian, H. Enquist, T. N. Hansen, A. Mikkelsen, P. Sondhauss, A. Srivastava, A. A. Zakharov, and J. Larsson. Repetitive ultrafast melting of insb as an x-ray timing diagnostic. *Journal of Applied Physics*, 103(10):103510, 2008.

[63] A. L. Cavalieri, D. M. Fritz, S. H. Lee, P. H. Bucksbaum, D. A. Reis, J. Rudati, D. M. Mills, P. H. Fuoss, G. B. Stephenson, C. C. Kao, D. P. Siddons, D. P. Lowney, A. G. MacPhee, D. Weinstein, R. W. Falcone, R. Pahl, J. Als-Nielsen, C. Blome, S. Düsterer, R. Ischebeck, H. Schlarb, H. Schulte-Schrepping, Th. Tschentscher, J. Schneider, O. Hignette, F. Sette, K. Sokolowski-Tinten, H. N. Chapman, R. W. Lee, T. N. Hansen, O. Synnergren, J. Larsson, S. Techert, J. Sheppard, J. S. Wark, M. Bergh, C. Caleman, G. Huldt, D. van der Spoel, N. Timneanu, J. Hajdu, R. A.

Akre, E. Bong, P. Emma, P. Krejcik, J. Arthur, S. Brennan, K. J. Gaffney, A. M. Lindenberg, K. Luening, and J. B. Hastings. Clocking femtosecond x rays. *Phys. Rev. Lett.*, 94:114801, Mar 2005.

[64] J. E. Sipe, Jeff F. Young, J. S. Preston, and H. M. van Driel. Laser-induced periodic surface structure. i. theory. *Phys. Rev. B*, 27:1141–1154, Jan 1983.

[65] A. Jurgilaitis, R. Nüske, H. Enquist, et al. X-ray diffraction from the ripple structures created by femtosecond laser pulses. *Appl. Phys. A*, 100:105–112, 2010.

[66] M. Harbst, T. Hansen, C. Caleman, et al. Studies of resolidification of non-thermally molten insb using time-resolved x-ray diffraction. *Appl. Phys. A*, 81:893–900, 2005.

[67] K. S. Novoselov, A. Mishchenko, A. Carvalho, and A. H. Castro Neto. 2d materials and van der waals heterostructures. *Science*, 353(6298), 2016.

[68] Peter Salén, Martina Basini, Stefano Bonetti, János Hebling, Mikhail Krasilnikov, Alexey Y. Nikitin, Georgii Shamuilov, Zoltán Tibai, Vitali Zhaunerchyk, and Vitaliy Goryashko. Matter manipulation with extreme terahertz light: Progress in the enabling thz technology. *Physics Reports*, 836-837:1 – 74, 2019. Matter manipulation with extreme terahertz light: Progress in the enabling THz technology.

[69] M. Kozina, T. van Driel, M. Chollet, T. Sato, J. M. Glownia, S. Wandel, M. Radovic, U. Staub, and M. C. Hoffmann. Ultrafast x-ray diffraction probe of terahertz field-driven soft mode dynamics in srtio3. *Structural Dynamics*, 4(5):054301, 2017.